UNIVERSIDAD DE CHILE
FACULTAD DE CIENCIAS FÍSICAS Y MATEMÁTICAS
DEPARTAMENTO DE FÍSICA

MAGNONS IN LOW-DIMENSIONAL COLLINEAR FERROMAGNETS

TESIS PARA OPTAR AL GRADO DE MAGÍSTER EN CIENCIAS, MENCIÓN FÍSICA

ESTEBAN JAVIER AGUILERA MARINOVIC

PROFESOR GUÍA:
ALVARO SESBASTIÁN NÚÑEZ VÁSQUEZ

MIEMBROS DE LA COMISIÓN:
LUIS E. F. FOÀ TORRES
RODRIGO ENRIQUE ARIAS FEDERICI
SIMÓN OYARZÚN MEDINA

Este trabajo ha sido parcialmente financiado por CEDENNA

SANTIAGO DE CHILE
2020

RESUMEN PARA OPTAR
AL GRADO DE: Magíster en Ciencias, mención Física
POR: Esteban Javier Aguilera Marinovic
FECHA: May 31, 2020
PROF. GUÍA: Álvaro Sebastián Núñez

MAGNONES EN FERROMAGNETOS COLINEALES DE BAJA DIMENSIONALIDAD

Esta tesis se centra en el estudio teórico de los magnones en el contexto de una red ferromagnética colineal en una y dos dimensiones. Este estudio se dedicó a dos modelos diferentes. El primer modelo busca comprender el comportamiento de los magnones en una monocapa de CrI_3. Mientras el segundo corresponde a un modelo de juguete unidimensional desarrollado para comprender el acoplamiento magnón-fonón que puede surgir debido a la existencia de un campo magnético que varía en el espacio.

En el primer capítulo, se presentan los antecedentes matemáticos necesarios para comprender los dos modelos analizados en esta tesis. El tema más crucial cubierto en este capítulo es la transformación de Holstein-Primakoff y su aplicación en la red de espín más general que encapsula cada sistema discutido en esta tesis. En este capítulo, también se resumen los métodos numéricos utilizados para resolver las energías propias y los estados propios de los sistemas bosónicos.

El segundo capítulo está dedicado al estudio de los magnones en una capa bidimensional de CrI_3. La descripción teórica de este sistema se realiza a través del modelo de Heisenberg-Kitaev, que se propuso recientemente como la teoría subyacente que describe su fenomenología. En este trabajo, se demuestra constructivamente que los magnones tienen una topología no trivial, y se realiza una predicción teórica del efecto Hall térmico, donde se muestra que el signo de la conductividad térmica de Hall depende de la temperatura del sistema.

En el último capítulo, se estudia la interacción entre magnones y fonones. La característica esencial de la teoría detrás de este capítulo es que la forma de un campo magnético, que varía en el espacio podría controlar el acoplamiento entre magnones y fonones. En este capítulo, se utilizan los datos conocidos del YIG para mostrar qué gradiente de campo magnético se necesita para obtener resultados comparables a los observados naturalmente en el mismo material debido al acoplamiento descrito fenomenológicamente por Kittel.

RESUMEN PARA OPTAR
AL GRADO DE: Magíster en Ciencias, mención Física
POR: Esteban Javier Aguilera Marinovic
FECHA: May 31, 2020
PROF. GUÍA: Álvaro Sebastián Núñez

MAGNONS IN LOW-DIMENSIONAL COLLINEAR FERROMAGNETS

This thesis is focused on the theoretical study of magnons in the context of one and two-dimensional collinear ferromagnetic lattice. This study was devoted to two different models. The first model seeks to understand the behavior of magnons in a monolayer of CrI_3. The second model is a unidimensional toy-model developed to understand magnon-phonon coupling that can emerge due to the existence of a space-varying magnetic field.

In the first chapter, the mathematical background needed to understand the two models analyzed in this thesis is introduced. The most crucial topic covered in this chapter is the Holstein-Primakoff transformation and its application in the most general spin-lattice that encapsulates every system discussed in this thesis. In this chapter, the numerical methods used to solve the eigenenergies and eigenstates of bosonic systems are also overviewed.

The second chapter is devoted to the study of magnons in a bidimensional layer of CrI_3. The theoretical description of this system is done through the Heisenberg-Kitaev model, which was recently proposed as the underlying theory that describes its phenomenology. In this work, it is constructively demonstrated that the magnons have non-trivial topology, and a theoretical prediction of the thermal Hall effect is performed, where it is shown that the sign of the thermal Hall conductivity depends on the temperature of the system.

In the last chapter, the interaction between magnons and phonons is studied. The essential feature of the theory behind this chapter is that the shape of a space-varying magnetic field could control the coupling between magnons and phonons. In this chapter, it is used data of YIG to show what magnetic field gradient is needed to obtain results comparable to the ones observed naturally in the same material due to the coupling described phenomenologically by Kittel.

To Consuelo

Contents

Chapter 1

Introduction

1.1 Heisenberg Model

Throughout this thesis, the work will be devoted to the study of collinear ferromagnets. These materials are magnetized, with a ground state in which every magnetized atomic site has a parallel magnetization relative to each other. The Heisenberg model [1] describes these materials effectively. This model considers that each site i, with spin $\boldsymbol{S}_i$, is coupled to each other site j through exchange interaction J_{ij}. Mathematically, the Hamiltonian of the system is:

$$\mathcal{H} = -\frac{1}{2}\sum_{i,j} J_{ij}\boldsymbol{S}_i \cdot \boldsymbol{S}_j - \mu_B g \sum_i \boldsymbol{B}_i \cdot \boldsymbol{S}_i \ . \tag{1.1}$$

In the literature [2], the Heisenberg model is usually understood just as the first term of equation 1.1, and it may also have the restriction that only nearest-neighboring interactions are considered. In this thesis, we will refer to the Heisenberg model to the systems that are described by stated Hamiltonian, where the second term is the Zeeman energy due to an external magnetic field $\boldsymbol{B}_i$ is also included [3].

Materials described by the proposed Hamiltonian can be studied either from a classical or quantum point of view. In the first case, the time evolution of the material's magnetization is given by the Landau-Lifschitz-Gilbert equation [4]:

$$\frac{\mathrm{d}\boldsymbol{M}_i}{\mathrm{d}t} = -\gamma \boldsymbol{M}_i \times \boldsymbol{h}_i - \lambda \boldsymbol{M}_i \times \left(\boldsymbol{M}_i \times \boldsymbol{h}_i\right) \ , \tag{1.2}$$

where,

$$h_i^\mu = -\frac{\delta \mathcal{H}}{\delta M_i^\mu} \tag{1.3}$$

and

$$\boldsymbol{M}_i = g\frac{q}{2m}\boldsymbol{S}_i \ . \tag{1.4}$$

Alternatively, from the quantum mechanical perspective, the system's dynamics are de-

scribed employing Heisenberg's picture [3]:

$$\frac{\mathrm{d}\boldsymbol{S}_i}{\mathrm{d}t} = \frac{\mathrm{i}}{\hbar}\big[\mathcal{H}, \boldsymbol{S}_i\big] \ . \tag{1.5}$$

Depending of the context, either equation 1.2 or equation 1.5 can be used to describe a material's dynamics. This thesis will not be about the resolution of the exact problem, meaning that the presented methods will not be employed. Instead, the focus of the study will be the behavior of quantized spin waves, called magnons.

1.2 Holstein-Primakoff

This section is devoted to the introduction of the Holstein-Primakoff transformation [5], which allows to transform spin variables such as the ones present in Hamiltonian 1.1 to variables that describe magnons. Before formally introducing the transformation, its important to remark that its main motivation is that the quantization of classical waves is achieved through second quantization [6]. In particular, they are described by bosoninc creation and annihilation operators, where one of the most common examples are photons [7] and phonons [2]. Following this spirit, the Holstein-Primakoff transformation takes us from spin operators $\boldsymbol{S}_i$ to bosonic operators a_i and $a_i^\dagger$, which describe the creation and annihilation of magnons in site i.

As it was previously mentioned, magnonic operators are bosons. This means that they must obey the commutation relations proper of bosons [8]:

$$\big[a_i, a_j\big] = 0 \tag{1.6a}$$

$$\big[a_i, a_j^\dagger\big] = \delta_{i,j} \ . \tag{1.6b}$$

And, in the case of our original spin operators $\boldsymbol{S}_i$, they must obey the angular momenta commutation relations [9]:

$$\big[S_i^\alpha, S_i^\beta\big] = \mathrm{i}\varepsilon_{\alpha\beta\gamma} S_i^\gamma \ . \tag{1.7}$$

Where summation over repeated indices is implied and it will be assumed throughout the thesis, unless stated otherwise.

To express spin operators as bosonic creation and annihilation operators, it is crucial that the corresponding commutation relations are preserved. In the seminal work by Holstein and Primakoff [5], it is shown that the transformation that preserves both commutation relations is:

$$S_i^+ = S_i^x + \mathrm{i}S_i^y = \sqrt{2S - a_i^\dagger a_i}\, a_i \tag{1.8a}$$

$$S_i^- = S_i^x - \mathrm{i}S_i^y = a_i^\dagger \sqrt{2S - a_i^\dagger a_i} \tag{1.8b}$$

$$S_i^z = S - a_i^\dagger a_i \ . \tag{1.8c}$$

Where S is the total spin of the site i.

As we have achieved our goal of transforming spin variables to bosonic variables, the most confortable spanning of the Hilbert space will not longer be the eigenvector of the spin

operators. The Hilbert space is completely spaned by a reduced Fock space, which is described by the eigenvectors $|n_i\rangle$ of the number operator $a_i^\dagger a_i$ with eigenvalues $n_i \in \{0, 1, ..., 2S\}$:

$$a_i^\dagger a_i \, |n_i\rangle = n_i \, |n_i\rangle \ . \tag{1.9}$$

With the Holstein-Primakoff transformation defined, it is time to be more accurate about its interpretation. From equation 1.8 it is direct to see that the operators $a_i^\dagger$ and a_i represent creation and annihilation of bosonic excitations away from the spin eigenstate $|s, s\rangle$. As it will be shown later, the excitations are not localized in the material. Thus, they are propagating through the material, giving them a wave-like behavior as it was expected from the initial intuition we developed [5].

Looking closely into equation 1.8, it is not clear how this may help to understand the behavior of magnons in the material, because of the difficulty of working with the square-root term. This problem can be sorted out if we work in the low magnon nuber limit, where we will have that $n_i << 2S$. Meaning that the operator $a_i^\dagger a_i$ can be treated as a small perturbation, allowing us to expand the term $\sqrt{2S - a_i^\dagger a_i}$ in series. To first order, the Holstein-Primakoff transformation can be approximated to:

$$S_i^+ \approx \sqrt{2S} a_i \tag{1.10a}$$

$$S_i^- \approx \sqrt{2S} a_i^\dagger \tag{1.10b}$$

$$S_i^z = S - a_i^\dagger a_i \ . \tag{1.10c}$$

An important detail that was not mentioned in the process to obtain equation 1.10, is that it was implicitly assumed that classicaly, the magnetization is constant and pointing in the $\hat{\boldsymbol{z}}$ throghout the whole material. To extend this approximation to a material with a magnetic texture $\boldsymbol{S}_0(\boldsymbol{r})$ or a noncollinear (anti)ferromagnet, a local system of coordinates $\{\hat{\boldsymbol{x}}_i', \hat{\boldsymbol{y}}_i', \hat{\boldsymbol{z}}_i'\}$ can be defined at each site i in such a way that $\hat{\boldsymbol{z}}_i' = \boldsymbol{S}_0(\boldsymbol{r}_i)/|\boldsymbol{S}_0(\boldsymbol{r}_i)|$ [10]. Mathematically, this change of coordinates can be simply introduced by means of rotation matrices:

$$\boldsymbol{S}_i' = \begin{pmatrix} \cos(\theta_i) & 0 & -\sin(\theta_i) \\ 0 & 1 & 0 \\ \sin(\theta_i) & 0 & \cos(\theta_i) \end{pmatrix} \cdot \begin{pmatrix} \cos(\phi_i) & \sin(\phi_i) & 0 \\ -\sin(\phi_i) & \cos(\phi_i) & 0 \\ 0 & 0 & 1 \end{pmatrix} \cdot \boldsymbol{S}_i \tag{1.11}$$

where the angles θ_i and ϕ_i are the spherical angles that describe spin texture locally: $\boldsymbol{S}_0(\boldsymbol{r}_i) = S\big(\sin(\theta_i)\cos(\phi_i), \sin(\theta_i)\sin(\phi_i), \cos(\theta_i)\big)$. For a more explicit discossion on this procedure please check reference [11].

1.3 Magnons in a One-dimensional Lattice

We will now proceed to show explicitly how the Holstein-Primakoff transformation allows us to understand the properties of magnons. For this, we will start by the simplest case we can consider, which is a one-dimensional spin-lattice with lattice constant a, as it is shown in figure 1.1. Mathematically, we will work in the particular case where Hamiltonian 1.1 consists of nearest-neighbor interactions. This means that the exchange interaction is given by:

$$J_{ij} = \begin{cases} J & \text{if } i = j \pm 1 \\ 0 & \sim \end{cases} \tag{1.12}$$

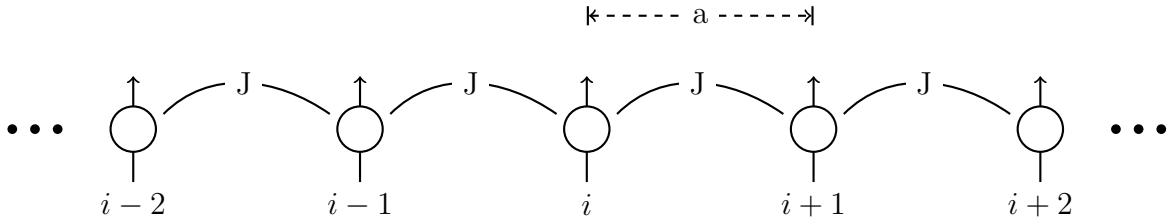

Figure 1.1: One-dimensional spin lattice with nearest-neighbor exchange coupling J and interatomic distance a. Magnons are studied around the equilibrium in the $\hat{\boldsymbol{z}}$ direction.

Replacing the exchange interaction in equation 1.12 to the original Hamiltonian (equation 1.1), one obtains:

$$\mathcal{H} = -J \sum_i \boldsymbol{S}_i \cdot \boldsymbol{S}_{i+1} - \mu_B g \sum_i \boldsymbol{B} \cdot \boldsymbol{S}_i \ . \tag{1.13}$$

Rewriting equation 1.10:

$$S_i^x = \sqrt{\frac{S}{2}}\left(a_i + a_i^\dagger\right) \ , \tag{1.14a}$$

$$S_i^y = -\mathrm{i}\sqrt{\frac{S}{2}}\left(a_i - a_i^\dagger\right) \ , \tag{1.14b}$$

$$S_i^z = S - a_i^\dagger a_i \ , \tag{1.14c}$$

and replacing them into equation 1.14 we obtain explicitly a Hamiltonian that allows us to directly study its linear magnons:

$$\begin{aligned} \mathcal{H}^{(m)} = -\frac{JS}{2} \sum_i \Bigg[& \left(a_i + a_i^\dagger\right)\left(a_{i+1} + a_{i+1}^\dagger\right) - \left(a_i - a_i^\dagger\right)\left(a_{i+1} - a_{i+1}^\dagger\right) - 2a_i^\dagger a_i \\ & - 2a_{i+1}^\dagger a_{i+1}\Bigg] - \mu_B g \sum_i \left[\sqrt{\frac{S}{2}} B^x \left(a_i + a_i^\dagger\right) - \mathrm{i}\sqrt{\frac{S}{2}} B^y \left(a_i - a_i^\dagger\right) - B^z a_i^\dagger a_i\right] . \end{aligned} \tag{1.15}$$

Reordering:

$$\begin{aligned} \Rightarrow \mathcal{H}^{(m)} = \sum_i \Bigg[& - JS\left(a_{i+1}^\dagger a_i + a_i^\dagger a_{i+1}\right) + \left(2JS + \mu_B g B^z\right) a_i^\dagger a_i \\ & - \sqrt{\frac{S}{2}} \mu_B g B^x \left(a_i + a_i^\dagger\right) + \mathrm{i}\sqrt{\frac{S}{2}} \mu_B g B^y \left(a_i - a_i^\dagger\right)\Bigg] \ . \end{aligned} \tag{1.16}$$

Reviewing what was done to obtain Hamiltonian 1.16, it is important to note that to obtain real magnons the magnetization in $\hat{\boldsymbol{z}}$, must be a classical stable equilibrium of the system. Otherwise, this magnons will decay as time passes and cease to exists. In this particular case, it is clear that the only way in which the $\hat{\boldsymbol{z}}$-direction is a stable equilibrium of the system is by having a magnetic field pointing in the same direction, which in turn cancels every linear term in Hamiltonian 1.16. This is no coincidence, as for every magnetic Hamiltonian its magnonic expansion around a stable texture will always give as a result that linear terms are zero. With this assumption, the Hamiltonian reads

$$\mathcal{H}^{(m)} = \sum_i \left[-JS\big(a_{i+1}^\dagger a_i + a_i^\dagger a_{i+1}\big) + \big(2JS + \mu_B g B_i^z\big) a_i^\dagger a_i \right] . \tag{1.17}$$

As with any Hamiltonian in quantum mechanics, we are interested in diagonalizing Hamiltonian 1.17. To accomplish this, we will make use of Bloch's theorem, which in terms of creation and annihilation operators can be expressed as

$$a_i = \frac{1}{\sqrt{N}} \sum_k a_k e^{\mathrm{i}kR_i} \ , \tag{1.18}$$

where $R_i = ia$.

Replacing equation 1.18 into equation 1.17 we obtain

$$\mathcal{H}^{(m)} = \sum_k \left[2JS\Big(1 - \cos(ka)\Big) + \mu_B g B^z \right] a_k^\dagger a_k \ . \tag{1.19}$$

From equation 1.19 it is direct that the dispersion relation is:

$$\epsilon_k = 2JS\Big(1 - \cos(ka)\Big) + \mu_B g B^z \ , \tag{1.20}$$

result that is ploted in figure 1.2.

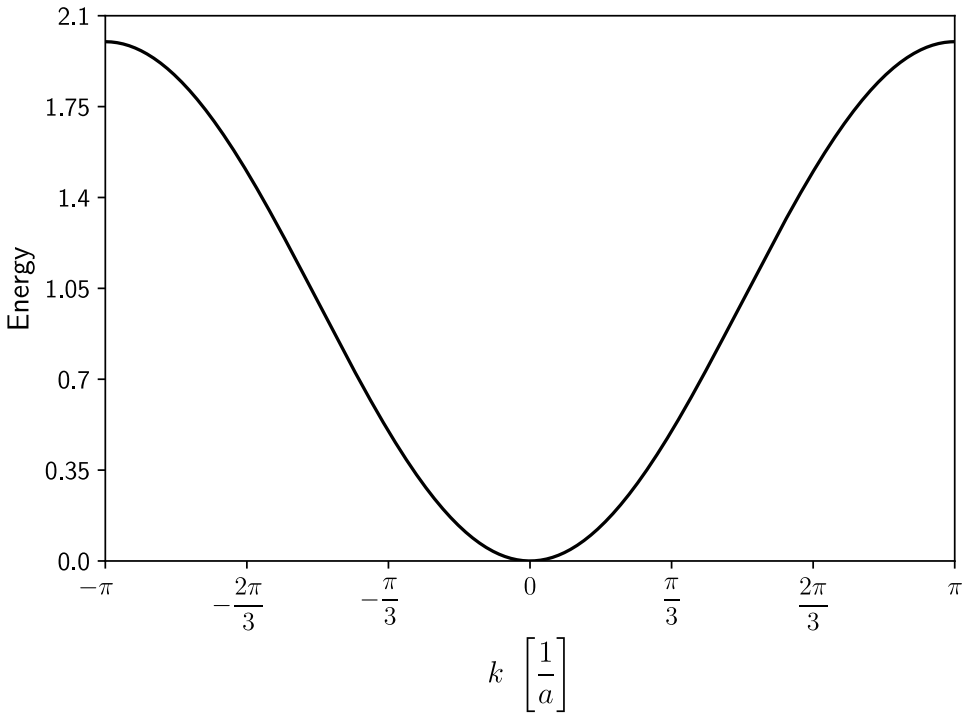

Figure 1.2: Dispersion relation for a one-dimensional spin lattice with nearest-neighbor Heisenberg exchange as obtained in equation 1.20. To obtain this plot the values used were $S = 1$, $J = 1$ and $B^z = 0$.

1.4 Magnons in Generalized Lattice

Throughout this thesis, we will work with different lattices with different basis. For this purpose, it is convenient to develop a general derivation of the Hamiltonian described by a basis of m sites, each with spin S_j, with $j \in \{0, 1, ..., m-1\}$. Each site that composes the basis of our lattice, there will exist an external magnetic field B_j and an easy-axis anisotropy A_j. Between two sites, described by the number of their unit cell $i, i' \in \{0, 1, ...N-1\}$ and specific site within our basis $j, j' \in \{0, 1, ...m-1\}$ there will exist an anisotropic exchange given by a tensor $J_{i-i'}^{jj'\alpha\beta}$, where we will use $i - i' \equiv \boldsymbol{R}_i - \boldsymbol{R}_{i'}$ and $\alpha, \beta \in \{x, y, z\}$. For the sake of completeness, we will also take into account a Dzyaloshinskii-Moriya interaction (DMI) term $\boldsymbol{D}_{i-i'}^{jj'}$, even though we will make use of it in the rest of the thesis. Mathematically speaking, this Hamiltonian is given by:

$$\begin{aligned}\mathcal{H} = &-\frac{1}{2}\sum_{ii'jj'} S_{ij}^{\alpha} J_{i-i'}^{jj'\alpha\beta} S_{i'j'}^{\beta} + \frac{1}{2}\sum_{ii'jj'} \boldsymbol{D}_{i-i'}^{jj'} \cdot \left(\boldsymbol{S}_{ij} \times \boldsymbol{S}_{i'j'}\right) - \sum_{ij} A_j \left(S_{ij}^{z}\right)^2 \\ &- \mu_B g \sum_{ij} \boldsymbol{B}_j \cdot \boldsymbol{S}_{ij} \ . \end{aligned} \tag{1.21}$$

From equation 1.21, it is desired to obtain a Hamiltonian for magnons in k-space using the same method developed in the previous section for the one-dimensional case. The first

step to achieve this is to use the linear Holstein-Primakoff transformation in its most general form, which is given by:

$$S_{ij}^{x} \approx \sqrt{\frac{S}{2}}\left(a_{ij}^{\dagger} + a_{ij}\right) \tag{1.22a}$$

$$S_{ij}^{y} \approx \mathrm{i}\sqrt{\frac{S}{2}}\left(a_{ij}^{\dagger} - a_{ij}\right) \tag{1.22b}$$

$$S_{ij}^{z} = S - a_{ij}^{\dagger}a_{ij} \ . \tag{1.22c}$$

Replacing the Holstein-Primakoff transformation into equation 1.21, it is obtained that the magnonic Hamiltonian in real space is:

$$\begin{aligned}\mathcal{H}^{(m)} = -\sum_{ii'jj'}\Bigg[&\frac{SJ_{i-i'}^{jj'xx}}{4}\left(a_{ij}^{\dagger}+a_{ij}\right)\left(a_{i'j'}^{\dagger}+a_{i'j'}\right)+\mathrm{i}\frac{SJ_{i-i'}^{jj'xy}}{4}\left(a_{ij}^{\dagger}+a_{ij}\right)\left(a_{i'j'}^{\dagger}-a_{i'j'}\right)\\&+\mathrm{i}\frac{SJ_{i-i'}^{jj'yx}}{4}\left(a_{ij}^{\dagger}-a_{ij}\right)\left(a_{i'j'}^{\dagger}+a_{i'j'}\right)-\frac{SJ_{i-i'}^{jj'yy}}{4}\left(a_{ij}^{\dagger}-a_{ij}\right)\left(a_{i'j'}^{\dagger}-a_{i'j'}\right)\\&-\frac{SJ_{i-i'}^{jj'zz}}{2}\left(a_{ij}^{\dagger}a_{ij}+a_{i'j'}^{\dagger}a_{i'j'}\right)\Bigg]+\sum_{ii'jj'}\Bigg[\mathrm{i}\frac{SD_{i-i'}^{jj'z}}{4}\Bigg(\left(a_{ij}^{\dagger}+a_{ij}\right)\left(a_{i'j'}^{\dagger}-a_{i'j'}\right)\\&-\left(a_{ij}^{\dagger}-a_{ij}\right)\left(a_{i'j'}^{\dagger}+a_{i'j'}\right)\Bigg)\Bigg]+\sum_{ij}\left(2SA_j+\mu_B g B_j^{z}\right)a_{ij}^{\dagger}a_{ij}\end{aligned} \tag{1.23}$$

which, can be reordered as

$$\begin{aligned}\mathcal{H}^{(m)} = -\frac{S}{4}\sum_{ii'jj'}\Bigg[&\Gamma_{i-i'}^{jj'-}a_{ij}^{\dagger}a_{i'j'}^{\dagger}+\left(\Gamma_{i-i'}^{jj'+}-2\mathrm{i}D_{i-i'}^{jj'z}\right)a_{ij}^{\dagger}a_{i'j'}+\left(\bar{\Gamma}_{i-i'}^{jj'+}+2\mathrm{i}D_{i-i'}^{jj'z}\right)a_{ij}a_{i'j'}^{\dagger}\\&+\bar{\Gamma}_{i-i'}^{jj'-}a_{ij}a_{i'j'}-2J_{i-i'}^{jj'zz}\left(a_{ij}^{\dagger}a_{ij}+a_{i'j'}^{\dagger}a_{i'j'}\right)\Bigg]+\sum_{ij}\left(2SA_j+\mu_B g B_j^{z}\right)a_{ij}^{\dagger}a_{ij}\ .\end{aligned} \tag{1.24}$$

Where, the following variables were defined:

$$\Gamma_{i-i'}^{jj'\pm} = J_{i-i'}^{jj'xx} \mp \mathrm{i}J_{i-i'}^{jj'xy} + \mathrm{i}J_{i-i'}^{jj'yx} \pm J_{i-i'}^{jj'yy} \tag{1.25a}$$

$$\bar{\Gamma}_{i-i'}^{jj'\pm} = J_{i-i'}^{jj'xx} \pm \mathrm{i}J_{i-i'}^{jj'xy} - \mathrm{i}J_{i-i'}^{jj'yx} \pm J_{i-i'}^{jj'yy} \ . \tag{1.25b}$$

Using Bloch's theorem for the creation and annihilation operators and the discrete Fourier transform for the anisotropic exchange and DMI:

$$a_{ij} = \frac{1}{\sqrt{N}}\sum_{k} a_{kj}e^{\mathrm{i}\boldsymbol{k}\cdot\boldsymbol{R}_{ij}} \tag{1.26a}$$

$$J_{i-i'}^{jj'\alpha\beta} = \frac{1}{N}\sum_{k} J_{k}^{jj'\alpha\beta}e^{\mathrm{i}\boldsymbol{k}\cdot(\boldsymbol{R}_{ij}-\boldsymbol{R}_{i'j'})} \tag{1.26b}$$

$$D_{i-i'}^{jj'\alpha} = \frac{1}{N}\sum_{k} D_{k}^{jj'\alpha}e^{\mathrm{i}\boldsymbol{k}\cdot(\boldsymbol{R}_{ij}-\boldsymbol{R}_{i'j'})} \ , \tag{1.26c}$$

can be used to obtain the Hamiltonian in $\boldsymbol{k}$-space:

$$\begin{aligned}\mathcal{H}^{(m)} = -\frac{S}{4}\sum_{jj'k}\Bigg[&\Gamma_k^{jj'-}a_{kj}^\dagger a_{-kj'}^\dagger + \bar{\Gamma}_k^{jj'-}a_{-kj}a_{kj'} + \left(\Gamma_k^{jj'+} - 2\mathfrak{i}D_k^{jj'z}\right)a_{kj}^\dagger a_{kj'} \\ &+ \left(\bar{\Gamma}_k^{jj'+} + 2\mathfrak{i}D_k^{jj'z}\right)a_{-kj}a_{-kj'}^\dagger - 2J_0^{jj'zz}\left(a_{kj}^\dagger a_{kj} + a_{kj'}^\dagger a_{kj'}\right)\Bigg] \\ &+ \sum_{jk}\left(2SA_j + \mu_B g B_j^z\right)a_{kj}^\dagger a_{kj}\ . \end{aligned} \tag{1.27}$$

Where the constants $\Gamma_k^{jj'\pm}$ and $\bar{\Gamma}_k^{jj'\pm}$ are defined through the inverse Fourier transform:

$$\Gamma_k^{jj'\pm} = \sum_{i-i'}\Gamma_{i-i'}^{jj'\pm}e^{-\mathfrak{i}\boldsymbol{k}\cdot(\boldsymbol{R}_{ij}-\boldsymbol{R}_{i'j'})} \tag{1.28a}$$

$$\bar{\Gamma}_k^{jj'\pm} = \sum_{i-i'}\bar{\Gamma}_{i-i'}^{jj'\pm}e^{-\mathfrak{i}\boldsymbol{k}\cdot(\boldsymbol{R}_{ij}-\boldsymbol{R}_{i'j'})} \tag{1.28b}$$

$$D_k^{jj'\alpha} = \sum_{i-i'}D_{i-i'}^{jj'\alpha}e^{-\mathfrak{i}\boldsymbol{k}\cdot(\boldsymbol{R}_{ij}-\boldsymbol{R}_{i'j'})}\ . \tag{1.28c}$$

To conclude this section, it is important to note that we have reduced the problem of finding the Hamiltonian in momentum space in to simply using equation 1.28 and replacing that result in equation 1.27. It is also worth noting, that in general, the Hamiltonian presented in equation 1.27 will not be diagonal, but one of our main interests throughout this thesis will be to find the eigenenergies and the associated eigenvectors. In the next section, we will introduce two different methods to obtain those values and make emphasize on the numerical implementation of both routines.

1.5 Diagonalization of a Quadratic Bosonic Hamiltonian

To introduce the diagonalization routined, we will be working with the most general quadratic Hamiltonian composed purely of m bosonic operators:

$$\mathcal{H} = \sum_{i,j}\left(T_{ij}\alpha_i^\dagger\alpha_j + \frac{1}{2}\left(U_{ij}\alpha_i\alpha_j + U_{ij}^*\alpha_i^\dagger\alpha_j^\dagger\right)\right) \tag{1.29a}$$

$$= \frac{1}{2}\begin{pmatrix}\boldsymbol{\alpha}^\dagger & \boldsymbol{\alpha}\end{pmatrix}\begin{pmatrix}T & U\\ U^* & T^*\end{pmatrix}\begin{pmatrix}\boldsymbol{\alpha}\\ \boldsymbol{\alpha}^\dagger\end{pmatrix}\ , \tag{1.29b}$$

where $\boldsymbol{\alpha} = \left(\alpha_0, \alpha_1, ..., \alpha_{m-1}\right)$ is a vector composed of the m bosonic operators.

We will understand diagonalization as the procedure through which m new bosonic operators γ_i are obtained such that they are linear combinations of the original creation and annihilation operators and the Hamiltonian takes the form [12]:

$$\mathcal{H} = \sum_{j=0}^{m-1}\omega_j\gamma_j^\dagger\gamma_j\ . \tag{1.30}$$

As we are dealing with a Hamiltonian that is purely described on bosons, the new operators γ_i must also satisfy the bosonic commutation relations. We will now show two methods in which we can obtain the diagonalization, both of which are different but equally valid whenever their assumptions are satisfied.

1.5.1 Bogoliubov Transformation

As it has already been stated, our goal is to find operators γ_i such that:

$$\left.\begin{aligned}\gamma_i &= A_{ij}\alpha_j + B_{ij}\alpha_j^\dagger \\ \gamma_i^\dagger &= B_{ij}^*\alpha_j + A_{ij}^*\alpha_j^\dagger\end{aligned}\right\} \quad \begin{pmatrix}\boldsymbol{\gamma} \\ \boldsymbol{\gamma}^\dagger\end{pmatrix} = \mathcal{T}\begin{pmatrix}\boldsymbol{\alpha} \\ \boldsymbol{\alpha}^\dagger\end{pmatrix} \ . \tag{1.31}$$

This, combined with the requirement that new operators also satisfies the bosonic commutation relations, we obtain that our solution must be restricted to:

$$AA^\dagger - BB^\dagger = \mathbb{1} \tag{1.32a}$$
$$AB^\intercal - BA^\intercal = \mathbb{0} \ . \tag{1.32b}$$

Where the first restriction of equation 1.32 comes from the fact that $[\gamma_i, \gamma_j^\dagger] = \delta_{i,j}$ and the second comes from $[\gamma_i, \gamma_j] = 0$. Both of this restrictions can be summarized in a single equation:

$$\begin{pmatrix}A & B \\ B^* & A^*\end{pmatrix}\begin{pmatrix}\mathbb{1} & \mathbb{0} \\ \mathbb{0} & -\mathbb{1}\end{pmatrix}\begin{pmatrix}A^\dagger & B^\intercal \\ B^\dagger & A^\intercal\end{pmatrix} = \begin{pmatrix}\mathbb{1} & \mathbb{0} \\ \mathbb{0} & -\mathbb{1}\end{pmatrix} \ . \tag{1.33}$$

Which can be reordered to show that the transformation presented in equation 1.31 cannot be a unitary one:

$$\begin{pmatrix}A & B \\ B^* & A^*\end{pmatrix}\begin{pmatrix}A^\dagger & -B^\intercal \\ -B^\dagger & A^\intercal\end{pmatrix} = \begin{pmatrix}\mathbb{1} & \mathbb{0} \\ \mathbb{0} & \mathbb{1}\end{pmatrix} \ . \tag{1.34}$$

Now, we can just replace the change of basis of equation 1.31 into the quadratic form of Hamiltonian 1.30 to show that the problem we need to solve is:

$$\begin{pmatrix}T & U \\ U^* & T^*\end{pmatrix} = \begin{pmatrix}A^\dagger & B^\intercal \\ B^\dagger & A^\intercal\end{pmatrix}\begin{pmatrix}\Omega & \mathbb{0} \\ \mathbb{0} & \Omega\end{pmatrix}\begin{pmatrix}A & B \\ B^* & A^*\end{pmatrix} \ . \tag{1.35}$$

Where Ω is a diagonal matrix. From this expression, it is important to note that equation 1.29 has a factor $1/2$ that has been canceled with the same factor that appears in the right-hand side of equation 1.35 hand because Ω appears twice.

Replacing equation 1.33 into equation 1.35 and reordering we obtain:

$$\begin{pmatrix}T & U \\ U^* & T^*\end{pmatrix} = \begin{pmatrix}\mathbb{1} & \mathbb{0} \\ \mathbb{0} & -\mathbb{1}\end{pmatrix}\begin{pmatrix}A^\dagger & -B^\intercal \\ -B^\dagger & A^\intercal\end{pmatrix}\begin{pmatrix}\mathbb{1} & \mathbb{0} \\ \mathbb{0} & -\mathbb{1}\end{pmatrix}\begin{pmatrix}\Omega & \mathbb{0} \\ \mathbb{0} & \Omega\end{pmatrix}\begin{pmatrix}A & B \\ B^* & A^*\end{pmatrix} \tag{1.36}$$

$$\Rightarrow \begin{pmatrix}\mathbb{1} & \mathbb{0} \\ \mathbb{0} & -\mathbb{1}\end{pmatrix}\begin{pmatrix}T & U \\ U^* & T^*\end{pmatrix} = \begin{pmatrix}A^\dagger & -B^\intercal \\ -B^\dagger & A^\intercal\end{pmatrix}\begin{pmatrix}\Omega & \mathbb{0} \\ \mathbb{0} & -\Omega\end{pmatrix}\begin{pmatrix}A & B \\ B^* & A^*\end{pmatrix} \ . \tag{1.37}$$

Noting closely, it is clear that the diagonalization problem for bosons is reduced to the diagonalization of the original Hamiltonian multiplied to the left by the para-unitary matrix.

When done numerically, it has to be done with care because the eigenvalues must be ordered so that they match their negative counterpart.

Although the presented algorithm does work as a diagonalization technique in the sense defined in equation 1.30 and it gives the correct eigenvalues, its eigenvectors are found in an inconvenient form because they do not meet the usually desired property that

$$\mathcal{T}^{\dagger}\mathcal{H}\mathcal{T} = diag\big(\omega_0, \omega_1, ..., \omega_{2m-1}\big) \ . \tag{1.38}$$

But, it is also important to note that this operation gives a diagonal matrix, but its elements are not the eigenvalues found in the matrix Ω.

1.5.2 Colpa's Algorithm

The second algorithm that can be used to diagonalize equation 1.29 is explained in its full extent in reference [12]. Here we will study the practical implementation of this algorithm and in the end, we will make a full comparison with the previously presented method. The main advantage this algorithm has to offer is that the obtained eigenvectors satisfy with equation 1.38. We will also limit our study to the particular case in which the Hamiltonian has the form:

$$\mathcal{H} = \frac{1}{2}\sum_{\boldsymbol{k}} \begin{pmatrix} \boldsymbol{\alpha}_{\boldsymbol{k}}^{\dagger} & \boldsymbol{\alpha}_{-\boldsymbol{k}} \end{pmatrix} H_{\boldsymbol{k}} \begin{pmatrix} \boldsymbol{\alpha}_{\boldsymbol{k}} \\ \boldsymbol{\alpha}_{-\boldsymbol{k}}^{\dagger} \end{pmatrix} \ . \tag{1.39}$$

Where $H_{\boldsymbol{k}}$ is a $(2m, 2m)$ matrix and $\boldsymbol{\alpha}_{\boldsymbol{k}} = \big(\alpha_{0\boldsymbol{k}}, \alpha_{1\boldsymbol{k}}, ..., \alpha_{m-1\boldsymbol{k}}\big)$.

As described in Colpa's original publication [12], we need for H_k to be a positive definite matrix to assure that it has real eigenvalues and the algorithm will only work when that assumption is true. The first step is to perform the Cholesky decomposition [13], which is defined as

$$H = WW^{\dagger} \ , \tag{1.40}$$

where W is a lower triangular matrix.

The algorithm continues by diagonalizing the matrix $W^{\dagger}\sigma_3 W$, where σ_3 is the para-unitary matrix. Here we obtain the diagonal matrix $\mathcal{L}$ with its eigenvalues and the matrix $\mathcal{U}$, where each column corresponds to an eigenvector. For the correct functioning of this algorithm, their eigenvalues and corresponding eigenvectors must be ordered in such a way that:

$$\mathcal{L} = diag\big(\omega_0, \omega_1, ..., \omega_{m-1}, -\omega_0, -\omega_1, ..., -\omega_{m-1}\big), \text{ with } \omega_0 \leqslant \omega_1 \leqslant ... \leqslant \omega_{m-1} \ . \tag{1.41}$$

With this we are ready to obtain the eigenvalues $\mathcal{E} = J\mathcal{L}$ and the transformation matrix $\mathcal{T}$, which is given by:

$$\mathcal{T} = \big(W^{\dagger}\big)^{-1}\mathcal{U}\sqrt{\mathcal{E}} \ . \tag{1.42}$$

As it was already mentioned, both algorithms return the same eigenvalues, but their eigenvectors are different. In the case of the first algorithm, we obtain normalized eigenvectors, while in Colpa's algorithm they are not normalized. They are also different in that the returned relative phase between each eigenvector is different with each algorithm.

Throughout this thesis, every numerical diagonalization will be done with Colpa's algorithm. Even though it is important to emphasize that in most calculations it does not matter which algorithm we choose. The only case where this matters is in the calculation of the Berry curvature done in Chapter 2.

Chapter 2

Topological Magnons in CrI_3

We will now focus our study of magnons in the two dimensional CrI_3 lattice. The material's monolayer was first reported in 2017 [14] and it was the first two-dimensional ferromagnet, with a Curie temperature of 45K. It is currently believed that the Cr atoms are the ones responsible for the magnetism in the material. This means that to study the magnetic properties of the material it should be enough to consider only the Cr atoms. If we take a look at figure 2.1, it can be seen that by taking into account only the Cr atoms, a honeycomb lattice is formed. This fact alone is a huge motivation to study in-depth magnons in CrI_3, because it has already been shown for different Hamiltonians for electrons in honeycomb lattice [15, 16], interesting (topological) properties may arise due to the geometrical properties of the honeycomb lattice.

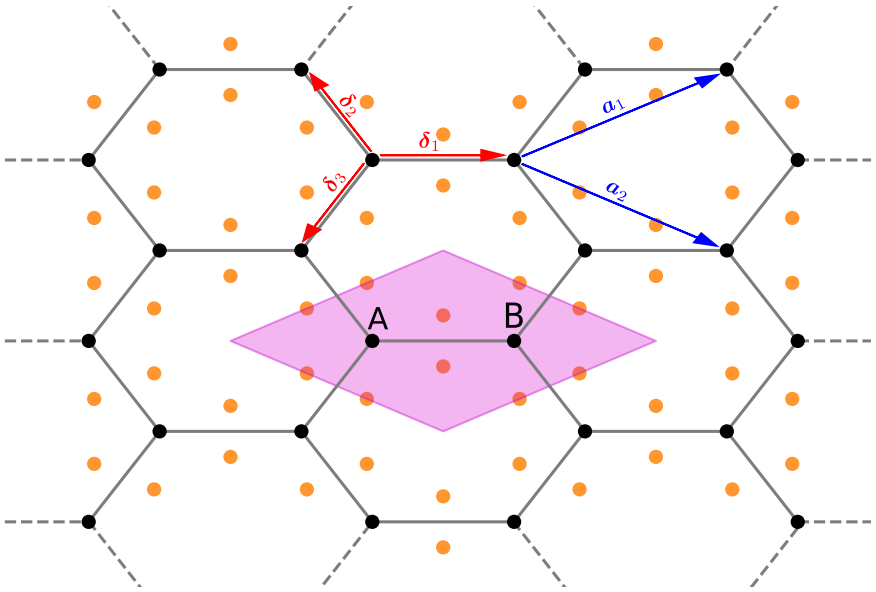

Figure 2.1: Bidimensional CrI_3 lattice seen from above. The Cr atoms are shown in black and the I atoms in grey. In pink we can see the unit cell, which is composed of two Cr atoms A and B and six I atoms.

We will begin the analysis of CrI_3 by stating the geometrical properties of a CrI_3 that we will be using in our study. As any honeycomb lattice, it has a basis composed of two atoms with nearest-neighbor distance $a = 4.07\text{Å}$. Relative to the unit cell's coordinates, the first one is in position $(0, 0, 0)$ and the second one in position $(a, 0, 0)$. The rest of the lattice can be formed by considering the following Bravais lattice vectors:

$$\boldsymbol{a_1} = \frac{\sqrt{3}a}{2}\begin{pmatrix}\sqrt{3}\\1\\0\end{pmatrix} \qquad \boldsymbol{a_2} = \frac{\sqrt{3}a}{2}\begin{pmatrix}\sqrt{3}\\-1\\0\end{pmatrix} \ . \tag{2.1}$$

It is also important to note that each site has three nearest-neighbors. Relative to a site $\boldsymbol{S}_a$, the position of its nearest-neighbors are:

$$\boldsymbol{\delta_1} = \begin{pmatrix}a\\0\\0\end{pmatrix} \qquad \boldsymbol{\delta_2} = \frac{a}{2}\begin{pmatrix}-1\\\sqrt{3}\\0\end{pmatrix} \qquad \boldsymbol{\delta_3} = \frac{a}{2}\begin{pmatrix}-1\\-\sqrt{3}\\0\end{pmatrix} \ . \tag{2.2}$$

To define the reciprocal lattice vectors $\boldsymbol{b}_i$, one must use the condition $\boldsymbol{a}_i \cdot \boldsymbol{b}_j = 2\pi\delta_{i,j}$. With this condition one obtains:

$$\boldsymbol{b_1} = \frac{2\pi}{3a}\begin{pmatrix}1\\\sqrt{3}\\0\end{pmatrix} \qquad \boldsymbol{b_2} = \frac{2\pi}{3a}\begin{pmatrix}1\\-\sqrt{3}\\0\end{pmatrix} \ . \tag{2.3}$$

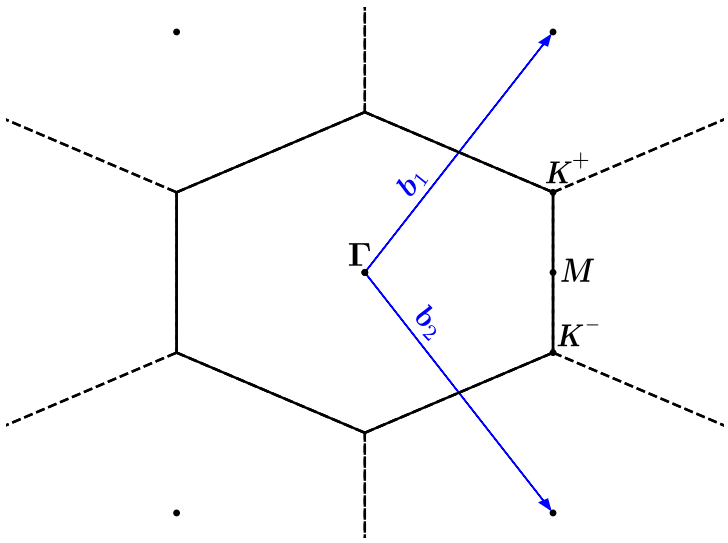

Figure 2.2: Wingner-Seitz cell produced by the reciprocal lattice. The highly symmetric points $\boldsymbol{\Gamma}$, $\boldsymbol{K}^+$ and $\boldsymbol{K}^-$ are also shown in the figure.

By building the first Brillouin zone (1BZ) as the Wigner-Seitz cell of the reciprocal lattice, one obtains a hexagonal-shaped 1BZ, as it is showed in figure 2.2. In the 1BZ there are four

important points called the highly symmetric points, which correspond to:

$$\boldsymbol{\Gamma} = \begin{pmatrix} 0 \\ 0 \\ 0 \end{pmatrix} \qquad \boldsymbol{M} = \frac{2\pi}{3a}\begin{pmatrix} 1 \\ 0 \\ 0 \end{pmatrix} \qquad \boldsymbol{K}^{+} = \frac{2\pi}{3\sqrt{3}a}\begin{pmatrix} \sqrt{3} \\ 1 \\ 0 \end{pmatrix} \qquad \boldsymbol{K}^{-} = \frac{2\pi}{3\sqrt{3}a}\begin{pmatrix} \sqrt{3} \\ -1 \\ 0 \end{pmatrix} . \tag{2.4}$$

To end with the geometrical considerations, we must notice from figure 2.3 that between two neighboring Cr sites, there exists a plane that is formed by Cr_2I_2. This plane changes for each nearest neighbor and a normal vector to each plane can be defined. For each nearest neighbor, we have that vector normal to the Cr_2I_2 plane are given by:

$$\hat{\boldsymbol{\gamma}}_1 = \frac{1}{\sqrt{3}}\begin{pmatrix} 0 \\ -\sqrt{2} \\ 1 \end{pmatrix} \qquad \hat{\boldsymbol{\gamma}}_2 = \frac{1}{\sqrt{6}}\begin{pmatrix} \sqrt{3} \\ 1 \\ \sqrt{2} \end{pmatrix} \qquad \hat{\boldsymbol{\gamma}}_3 = \frac{1}{\sqrt{6}}\begin{pmatrix} -\sqrt{3} \\ -1 \\ \sqrt{2} \end{pmatrix} \tag{2.5}$$

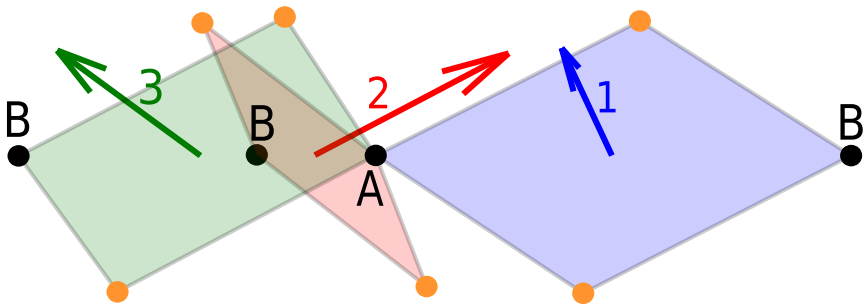

Figure 2.3: Side view of CrI_3. Where only one type-A Cr site is included and its three nearest Cr. In blue, red and green we can see the three possible Cr_2I_2 planes and their respective normal vectors $\hat{\boldsymbol{\gamma}}_1$, $\hat{\boldsymbol{\gamma}}_2$ and $\hat{\boldsymbol{\gamma}}_3$.

With all these geometrical properties of CrI_3 we can begin with the analysis of magnons in CrI_3. In the existing literature, the material has been extensively studied as a Honeycomb ferromagnet described by a nearest-neighbor Heisenberg interaction and next-nearest-neighbor DMI [17, 18]. Where its main prediction is the existence of topological magnons. Recently, it has been proposed as an alternative model to CrI_3 a Honeycomb ferromagnet described by a nearest-neighbor Heisenberg-Kitaev interaction. In the next section, we are going to introduce this model and show explicitly what is the resulting magnonic Hamiltonian for this particular case.

2.1 Heisenberg-Kitaev Model

The Heisenberg-Kitaev model consist of the usual Heisenberg Hamiltonian presented in equation 1.1 with an aditional anisotropic term that comes from the Kitaev model [19]. This way, CrI_3 will be modeled as a Honeycomb spin lattice with the Hamiltonian:

$$\mathcal{H} = -\sum_{<i,j>}\left[J\boldsymbol{S}_i\cdot\boldsymbol{S}_j + K\left(\boldsymbol{S}_i\cdot\hat{\boldsymbol{\gamma}}_{\boldsymbol{\delta}}\right)\left(\boldsymbol{S}_j\cdot\hat{\boldsymbol{\gamma}}_{\boldsymbol{\delta}}\right)\right] - A\sum_i\left(S_i^z\right)^2 . \tag{2.6}$$

Where $\hat{\boldsymbol{\gamma}}_{\boldsymbol{\delta}}$ is the direction upon which the the Kitaev parameter is acting, which depends directly on the link $\boldsymbol{\delta} \equiv \boldsymbol{R}_i - \boldsymbol{R}_j$ we are dealing with. In the case of CrI_3, they are precisely the vectors normal to the Cr_2I_2 planes defined in equation 2.5.

The clearer way to make this analysis is to write Hamiltonian 2.6 with a unique exchange tensor $J^{\mu\nu}$, represented in the basis defined by the vectors $\hat{\boldsymbol{\gamma}}_{\boldsymbol{\delta}}$:

$$J^{\mu\nu} = \begin{pmatrix} J & 0 & 0 \\ 0 & J & 0 \\ 0 & 0 & J+K \end{pmatrix} . \tag{2.7}$$

The problem with the coordinate system of equation 2.7 is that it will be different for the three possible links. This issue can be sorted by using the rotation matrices $R_{\boldsymbol{\delta}}$, defined as those that allow us to transform from $\hat{\boldsymbol{\gamma}}_{\boldsymbol{\delta}}$ to $\hat{\boldsymbol{z}}$:

$$\hat{\boldsymbol{z}} = R_{\boldsymbol{\delta}} \cdot \hat{\boldsymbol{\gamma}}_{\boldsymbol{\delta}} \equiv \begin{pmatrix} \cos(\theta_{\boldsymbol{\delta}}) & 0 & -\sin(\theta_{\boldsymbol{\delta}}) \\ 0 & 1 & 0 \\ \sin(\theta_{\boldsymbol{\delta}}) & 0 & \cos(\theta_{\boldsymbol{\delta}}) \end{pmatrix} \cdot \begin{pmatrix} \cos(\phi_{\boldsymbol{\delta}}) & \sin(\phi_{\boldsymbol{\delta}}) & 0 \\ -\sin(\phi_{\boldsymbol{\delta}}) & \cos(\phi_{\boldsymbol{\delta}}) & 0 \\ 0 & 0 & 1 \end{pmatrix} \hat{\boldsymbol{\gamma}}_{\boldsymbol{\delta}} . \tag{2.8}$$

Where we are considering that $\theta_{\boldsymbol{\delta}}$ and $\phi_{\boldsymbol{\delta}}$ are the spherical coordinate angles that describe $\hat{\boldsymbol{\gamma}}_{\boldsymbol{\delta}}$.

Using equation 2.8, we can transform the exchange interaction $J^{\mu\nu}$ in the link-dependent coordinate system to an link-dependent exchange interaction $\mathcal{J}_{\boldsymbol{\delta}}^{\alpha\beta}$ described in the usual $\{x, y, z\}$ basis, where $\hat{\boldsymbol{z}}$ is the out-of-plane axis to the bidimensional lattice:

$$\mathcal{J}_{\boldsymbol{\delta}} = R_{\boldsymbol{\delta}}^{\intercal} J R_{\boldsymbol{\delta}} . \tag{2.9}$$

Using this change of coordinates to write $\mathcal{J}_{\boldsymbol{\delta}}^{\alpha\beta}$, we obtain that Hamiltonian 2.6 can be rewritten as:

$$H = -\sum_{\substack{i \\ j \in nn(i)}} S_{ia}^{\alpha} \mathcal{J}_{\boldsymbol{\delta}}^{\alpha\beta} S_{jb}^{\beta} - \sum_{i,\sigma} A \cdot \left(S_{i\sigma}^{z}\right)^2 . \tag{2.10}$$

Where the index i goes through all the unit cells, j are the neighboring unit cells and lastly, $\sigma \in \{a, b\}$ points the particular site of the honeycomb lattice basis we are dealing with.

As it was previously mentioned, our objective is to understand the nature of magnons in the Kitaev model for CrI_3. To obtain the Hamiltonian for magnons in $\boldsymbol{k}$-space, we could just use equation 1.27. This method would not yield a clear form of the bulk's Hamiltonian, which is going to make its analytical analysis more cumbersome. Because of this reason is that we are going to realize this description from scratch and reserve equation 1.27 for section 2.3, when we analyze the eigenenergies and eigenstates of the nanoribbon.

To obtain the Hamiltonian for magnons, we must begin by using Holstein-Primakoff's

transformation. Which is given by:

$$S_{ia}^{(x)} = \sqrt{\frac{S}{2}}\left(a_i^\dagger + a_i\right) \qquad S_{ib}^{(x)} = \sqrt{\frac{S}{2}}\left(b_i^\dagger + b_i\right) \tag{2.11a}$$

$$S_{ia}^{(y)} = \mathrm{i}\sqrt{\frac{S}{2}}\left(a_i^\dagger - a_i\right) \qquad S_{ib}^{(y)} = \mathrm{i}\sqrt{\frac{S}{2}}\left(b_i^\dagger - b_i\right) \tag{2.11b}$$

$$S_{ia}^{(z)} = S - a_i^\dagger a_i \qquad S_{ib}^{(z)} = S - b_i^\dagger b_i \ . \tag{2.11c}$$

Replacing the transformation into equation 2.10, we obtain

$$\begin{aligned}\mathcal{H} = \frac{S}{2}\sum_{\substack{i\\ j\in nn(i)}}\Bigg[&-\left(\mathcal{J}_{\boldsymbol{\delta}}^{xx} - \mathrm{i}\mathcal{J}_{\boldsymbol{\delta}}^{xy} - \mathrm{i}\mathcal{J}_{\boldsymbol{\delta}}^{yx} - \mathcal{J}_{\boldsymbol{\delta}}^{yy}\right)a_i b_j \\ &-\left(\mathcal{J}_{\boldsymbol{\delta}}^{xx} + \mathrm{i}\mathcal{J}_{\boldsymbol{\delta}}^{xy} - \mathrm{i}\mathcal{J}_{\boldsymbol{\delta}}^{yx} + \mathcal{J}_{\boldsymbol{\delta}}^{yy}\right)a_i b_j^\dagger - \left(\mathcal{J}_{\boldsymbol{\delta}}^{xx} - \mathrm{i}\mathcal{J}_{\boldsymbol{\delta}}^{xy} + \mathrm{i}\mathcal{J}_{\boldsymbol{\delta}}^{yx} + \mathcal{J}_{\boldsymbol{\delta}}^{yy}\right)a_i^\dagger b_j \\ &-\left(\mathcal{J}_{\boldsymbol{\delta}}^{xx} + \mathrm{i}\mathcal{J}_{\boldsymbol{\delta}}^{xy} + \mathrm{i}\mathcal{J}_{\boldsymbol{\delta}}^{yx} - \mathcal{J}_{\boldsymbol{\delta}}^{yy}\right)a_i^\dagger b_j^\dagger + 2\mathcal{J}_{\boldsymbol{\delta}}^{zz}\left(a_i^\dagger a_i + b_j^\dagger b_j\right)\Bigg] + 2AS\sum_i\left(a_i^\dagger a_i + b_i^\dagger b_i\right) \ . \end{aligned} \tag{2.12}$$

To further simplify equation 2.12, we will use the fact that the anisotropic exchange is symmetric $\left(J_{\boldsymbol{\delta}}^{\alpha\beta} = J_{\boldsymbol{\delta}}^{\beta\alpha}\right)$, meaning that we obtain:

$$\begin{aligned}\mathcal{H} = \frac{S}{2}\sum_{\substack{i\\ j\in nn(i)}}\Bigg[&-\left(\mathcal{J}_{\boldsymbol{\delta}}^{xx} + \mathcal{J}_{\boldsymbol{\delta}}^{yy}\right)a_i b_j^\dagger - \left(\mathcal{J}_{\boldsymbol{\delta}}^{xx} + \mathcal{J}_{\boldsymbol{\delta}}^{yy}\right)a_i^\dagger b_j - \left(\mathcal{J}_{\boldsymbol{\delta}}^{xx} - \mathcal{J}_{\boldsymbol{\delta}}^{yy} - \mathrm{i}2\mathcal{J}_{\boldsymbol{\delta}}^{xy}\right)a_i b_j \\ &-\left(\mathcal{J}_{\boldsymbol{\delta}}^{xx} - \mathcal{J}_{\boldsymbol{\delta}}^{yy} + \mathrm{i}2\mathcal{J}_{\boldsymbol{\delta}}^{xy}\right)a_i^\dagger b_j^\dagger + 2\mathcal{J}_{\boldsymbol{\delta}}^{zz}\left(a_i^\dagger a_i + b_j^\dagger b_j\right)\Bigg] + 2AS\sum_i\left(a_i^\dagger a_i + b_i^\dagger b_i\right) \ . \end{aligned} \tag{2.13}$$

From equation 2.13 we will proceed by using Bloch's theorem in a_i and b_i, to obtain the Hamiltonian in $\boldsymbol{k}$-space:

$$\begin{aligned}\mathcal{H} = \frac{S}{2}\sum_{\boldsymbol{k},\boldsymbol{\delta}}\Bigg[&-\left(\mathcal{J}_{\boldsymbol{\delta}}^{xx} + \mathcal{J}_{\boldsymbol{\delta}}^{yy}\right)\left(e^{\mathrm{i}\boldsymbol{k}\cdot\boldsymbol{\delta}}a_{\boldsymbol{k}}^\dagger b_{\boldsymbol{k}} + e^{-\mathrm{i}\boldsymbol{k}\cdot\boldsymbol{\delta}}b_{\boldsymbol{k}}^\dagger a_{\boldsymbol{k}}\right) - \left(\mathcal{J}_{\boldsymbol{\delta}}^{xx} - \mathcal{J}_{\boldsymbol{\delta}}^{yy} - 2\mathrm{i}\mathcal{J}_{\boldsymbol{\delta}}^{xy}\right)e^{-\mathrm{i}\boldsymbol{k}\cdot\boldsymbol{\delta}}a_{\boldsymbol{k}}b_{-\boldsymbol{k}} \\ &-\left(\mathcal{J}_{\boldsymbol{\delta}}^{xx} - \mathcal{J}_{\boldsymbol{\delta}}^{yy} + 2\mathrm{i}\mathcal{J}_{\boldsymbol{\delta}}^{xy}\right)e^{\mathrm{i}\boldsymbol{k}\cdot\boldsymbol{\delta}}b_{-\boldsymbol{k}}^\dagger a_{\boldsymbol{k}}^\dagger + 2\mathcal{J}_{\boldsymbol{\delta}}^{zz}\left(a_{\boldsymbol{k}}^\dagger a_{\boldsymbol{k}} + b_{\boldsymbol{k}}^\dagger b_{\boldsymbol{k}}\right)\Bigg] + 2AS\sum_{\boldsymbol{k}}\left(a_{\boldsymbol{k}}^\dagger a_{\boldsymbol{k}} + b_{\boldsymbol{k}}^\dagger b_{\boldsymbol{k}}\right) \ . \end{aligned} \tag{2.14}$$

2.2 Bulk's dispersion relation

Now, we are ready to write equation 2.14 in a quadratic form and use Colpa's Algorithm to obtain the eigenenergies. In figure 2.4 we can see the bulk dispersion relation for CrI_3 for $K = 0$meV and $K = 4.07$meV, which is a value that has been suggested in recent publications [20]. Both plots were made by considering the path in $\boldsymbol{k}$-space that starts in $\boldsymbol{\Gamma}$, passes through $\boldsymbol{M}$, $\boldsymbol{K}^+$ and ends back in $\boldsymbol{\Gamma}$. It is also important that in this figure

and throughout this entire section, a Heisenberg exchange of $J = 0.53$meV and an easy-axis anisotropy of $A = 0.44$meV [20, 21].

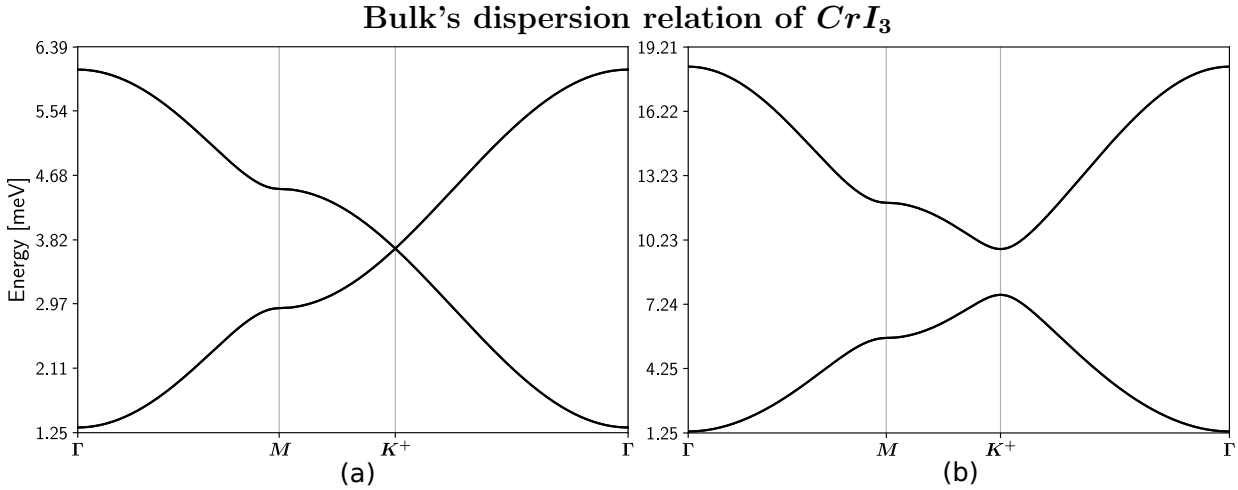

Figure 2.4: Bulk's dispersion relation for CrI_3 with $J = 0.53$meV and $A = 0.44$meV. **(a)** Case with $K = 0$, where there is no energy gap between the two bands. **(b)** corresponds to the case with $K = 4.07$meV, where it can be seen that a gap opens at $\boldsymbol{K}^+$.

Comparing both dispersion relations in figure 2.4 it can be seen that a gap opens $K = 4.07$meV at the point $\boldsymbol{K}^+$, and the same can be checked for the point $\boldsymbol{K}^-$. As it can be seen from figure 2.5, where we plot the value of the energy gap at point $\boldsymbol{K}^+$ for different values of K, this gap only closes for $K = 0$, which corresponds to describing the material with a pure Heisenberg model.

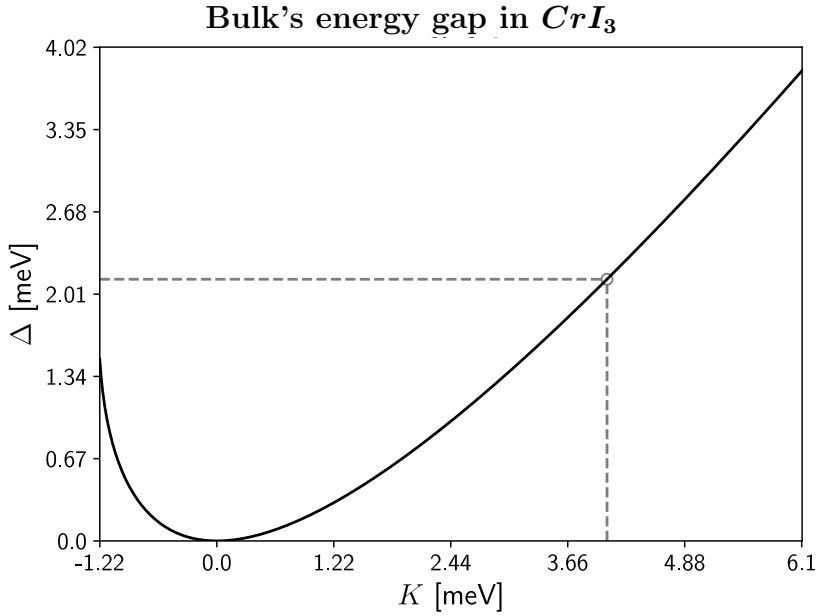

Figure 2.5: Gap between the lower and upper band of CrI_3 at point $\boldsymbol{K}^+$ for different values of K. From this plot it is clear that the gap only closes for $K = 0$. The energy gap for $K = 4.07$meV has been highlighted, as it is the value most commonly used throughout the chapter.

In tight-binding models, it is common to see the appearance of gaps when a new term is incorporated into the bulk Hamiltonian of a material. When this occurs, it is not uncommon to think that this might lead to topologically protected states, though the appearance of a gap does not imply directly that we are dealing with topologically protected states. As an example, we can take graphene with the nearest-neighbor hopping. A gap will open if we have that the on-site energies are different for sites a and b but, this gap leads to topologically trivial states. Another way of opening a gap in graphene is by adding a complex next-nearest neighbor hopping [15], where the resulting eigenstates lead to topologically protected edge states with non-zero Chern number.

The similarity between equation 2.14 and electronic tight-binding Hamiltonians is clear. So, because a gap opening could be of topological topological nature, we will undertake the task of studying thism and show that topological states will indeed appear.

To demonstrate that the gap is indeed topological, we will start by analyzing a nanoribbon. In this case, we expect the same behavior it is seen in topological states in tight-binding models. This means that there should exist a band that goes from the lower set of bands to the upper set of bands and the eigenstates corresponding to those energies should be located in the boundary of the nanoribbon.

2.3 Nanoribbons

To study nanoribbons we must start by choosing a border for the honeycomb lattice. To begin this analysis we will begin studying the zig-zag border. Because of the existence of a finite border, we will have only one lattice vector

$$\boldsymbol{\alpha} = \left(0, \sqrt{3}\, a, 0\right) \tag{2.15}$$

and a unit cell with a basis composed of m distinct but identical sites as shown on figure 2.6.

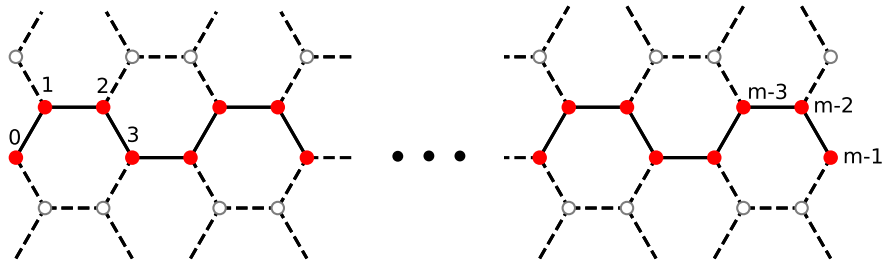

Figure 2.6: CrI_3 nanoribbon with zigzag border.

To obtain the eigenenergies and eigenstates of the nanoribbon we will make use of equation 1.27 and Colpa's algorithm. This means that we need to start by calculating $J_k^{jj'}$. To accomplish this, we will start by noticing that in real space we have that:

$$J_{i-i'}^{jj'\alpha\beta} = \begin{cases} \left(\mathcal{J}_3^{\alpha\beta}\delta_{i-i',0} + \mathcal{J}_2^{\alpha\beta}\delta_{i-i',-\boldsymbol{a}}\right)\delta_{j,j'+1} + \mathcal{J}_1^{\alpha\beta}\delta_{i-i',0}\delta_{j,j'-1} & \text{if j is odd} \\ \left(\mathcal{J}_3^{\alpha\beta}\delta_{i-i',0} + \mathcal{J}_2^{\alpha\beta}\delta_{i-i',\boldsymbol{a}}\right)\delta_{j,j'-1} + \mathcal{J}_1^{\alpha\beta}\delta_{i-i',0}\delta_{j,j'+1} & \text{if j is even .} \end{cases} \tag{2.16}$$

Where we are using the same notation used before, where $i - i' \equiv \boldsymbol{R}_i - \boldsymbol{R}_{i'}$. Using the inverse fourier transform defined from equation 1.26 we obtain:

$$J_k^{jj'\alpha\beta} = \begin{cases} \left(\mathcal{J}_3^{\alpha\beta} + \mathcal{J}_2^{\alpha\beta} e^{\mathrm{i}\boldsymbol{k}\cdot\boldsymbol{\alpha}}\right)\delta_{j,j'+1} + \mathcal{J}_1^{\alpha\beta}\delta_{j,j'-1} & \text{if j is odd} \\ \left(\mathcal{J}_3^{\alpha\beta} + \mathcal{J}_2^{\alpha\beta} e^{-\mathrm{i}\boldsymbol{k}\cdot\boldsymbol{\alpha}}\right)\delta_{j,j'-1} + \mathcal{J}_1^{\alpha\beta}\delta_{j,j'+1} & \text{if j is even .} \end{cases} \tag{2.17}$$

With equation 2.17 we are ready to use Colpa's algorithm to obtain the eigenenergies and eigenvalues of the zigzag nanoribbon. Considering the same values used to obtain figure 2.4 the dispersion relations in figure 2.7 are obtained. In blue, the bulk's gap has been marked. A single band crosses through it, which is a main hint that there could be topological edge states.

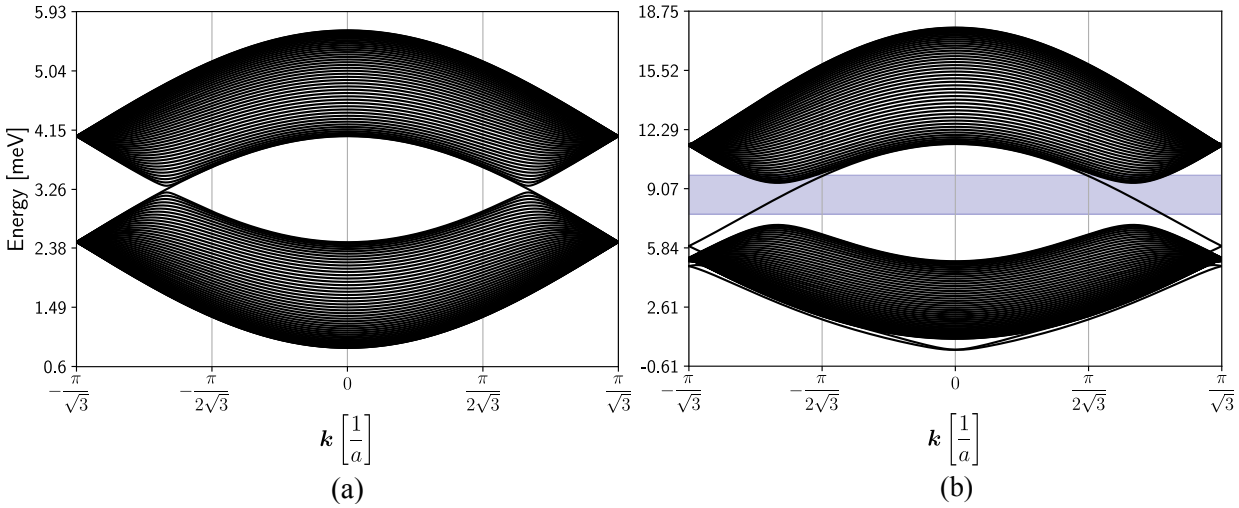

Figure 2.7: Dispersion relation of the CrI_3 nanoribbon with $m = 100$ sites of width. **(a)** Case with $K = 0$, where the small gap between the top and lower set of bands due to finiteness effects. **(b)** Case with K=4.07meV, where the bulk's gap is marked in blue. It is also important to notice that in this situation the gap of the nanoribbon is bigger and the band that crosses from one set of bands to the other is also the only one that crosses the bulk's gap.

To obtain a better picture of the nanoribbon, the eigenergies and eigenstates for a nanoribbon with $m = 20$ sites of width are plotted in figure 2.8. In this figure we find plotted the eigenstates for the two states that cross the gap in the nanoribbon, where the radii of the grey circles shows the probability of finding the magnon in a particular site. From this plot, it is clear that there is no edge-localization in the left panel, where we have that $K = 0$. On the other hand, in the right panel, where $K = 4.07$meV, we find one state localized in the left border and the other on the right border.

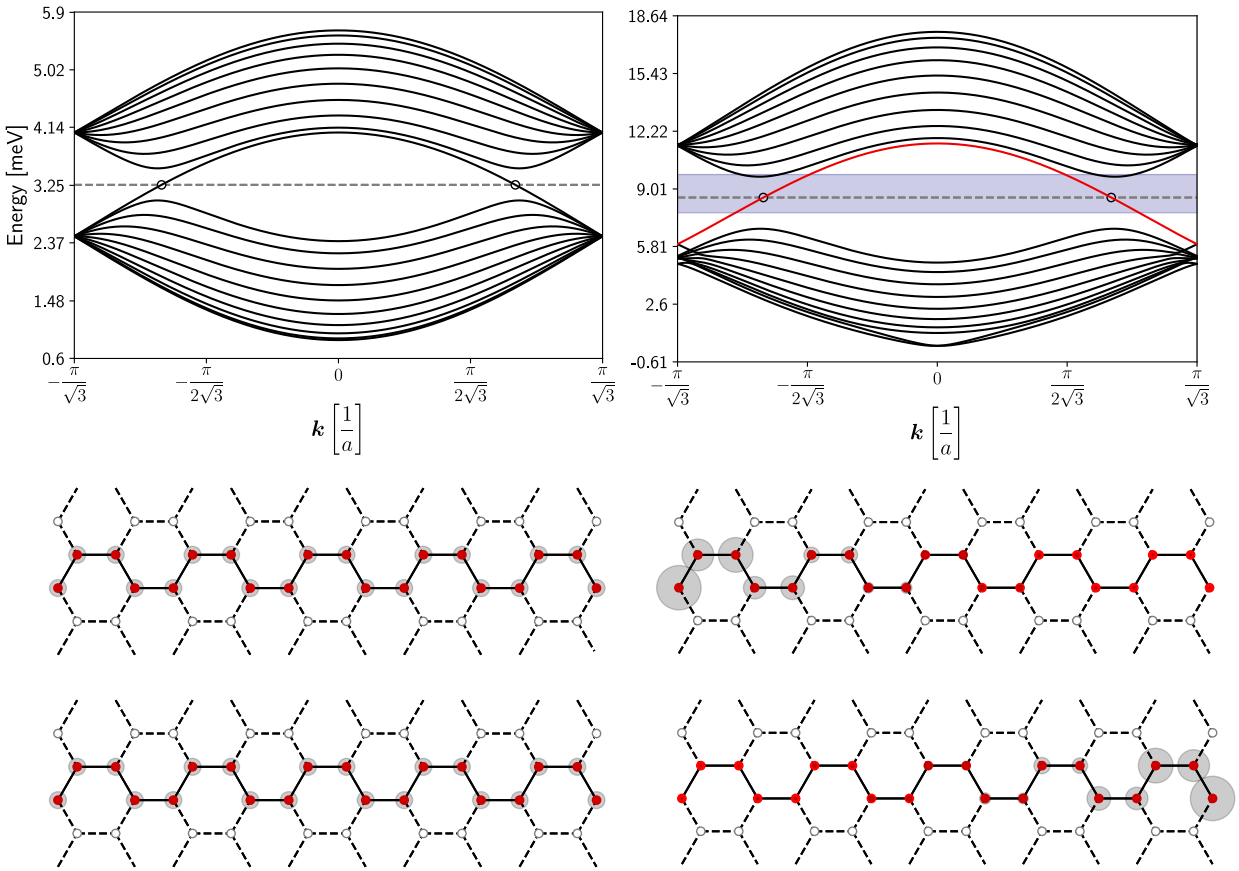

Figure 2.8: Dispersion relation and states corresponding to the marked energies for the zigzag nanoribbon. **Left Panel:** Situation with $K = 0$. There is a resemblance with graphene, where two of the top bands lower their energies due to the on-site energy discrepancy at the edge. The plots below represent the magnitude of the probabilities for the two possible states with $E = 3.26$meV. The probability is proportional to the radii of the grey circles. **Right Panel:** Situation with $K = 4.07$meV. Bands preserve their basic structure and the two central bands are separated. The light-blue colored area is the gap of the bulk, which shows which band should have a topological behavior. The lower plots represent the probability of the states with $E = 8.53$meV. There is a clear localization at both edges of the ribbon.

The analysis performed on figure 2.8 can also be performed in the case where the nanoribbon has armchair borders. In this case we have a unit cell with m sites, as it is shown on figure 2.9.

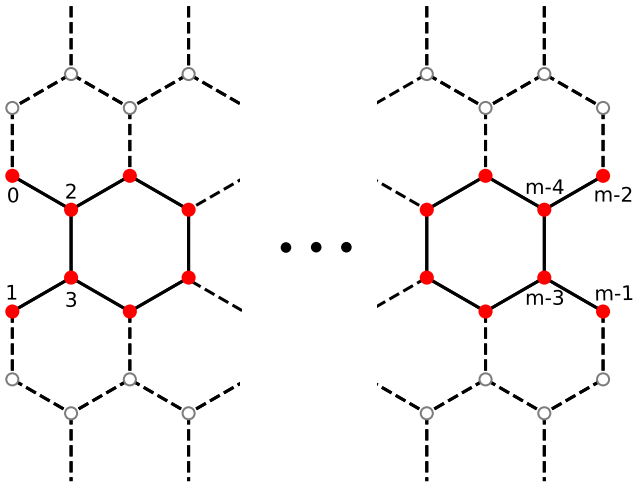

Figure 2.9: CrI_3 nanoribbon with armchair border.

In this case, we have the exchange tensor in $\boldsymbol{k}$-space is given by:

$$J_{\boldsymbol{k}}^{jj'\alpha\beta} = \begin{cases} \mathcal{J}_1^{\alpha\beta} e^{i\boldsymbol{k}\cdot\boldsymbol{\alpha}} \delta_{j,j'-1} + \mathcal{J}_2^{\alpha\beta} \delta_{j,j'+2} + \mathcal{J}_3^{\alpha\beta} \delta_{j,j'-2} & \text{if j} = 4\text{n} \\ \mathcal{J}_1^{\alpha\beta} e^{-i\boldsymbol{k}\cdot\boldsymbol{\alpha}} \delta_{j,j'+1} + \mathcal{J}_2^{\alpha\beta} \delta_{j,j'-2} + \mathcal{J}_3^{\alpha\beta} \delta_{j,j'+2} & \text{if j} = 4\text{n+1} \\ \mathcal{J}_1^{\alpha\beta} \delta_{j,j'-1} + \mathcal{J}_2^{\alpha\beta} \delta_{j,j'-2} + \mathcal{J}_3^{\alpha\beta} \delta_{j,j'+2} & \text{if j} = 4\text{n+2} \\ \mathcal{J}_1^{\alpha\beta} \delta_{j,j'+1} + \mathcal{J}_2^{\alpha\beta} \delta_{j,j'+2} + \mathcal{J}_3^{\alpha\beta} \delta_{j,j'-2} & \text{if j} = 4\text{n+3} \ . \end{cases} \tag{2.18}$$

With this, the obtained eigenenergies and eigenstates are shown on figure 2.10. In this figure we can check that, similar to the zigzag case, there are no chiral edge-states in the case where $K = 0$ (left panel) in the artificial gap produced be the finiteness of the gap. In the case with $K = 4.07$meV (right panel) the chiral edge-states do exist in the states corresponding to the energies inside the bulk's energy gap.

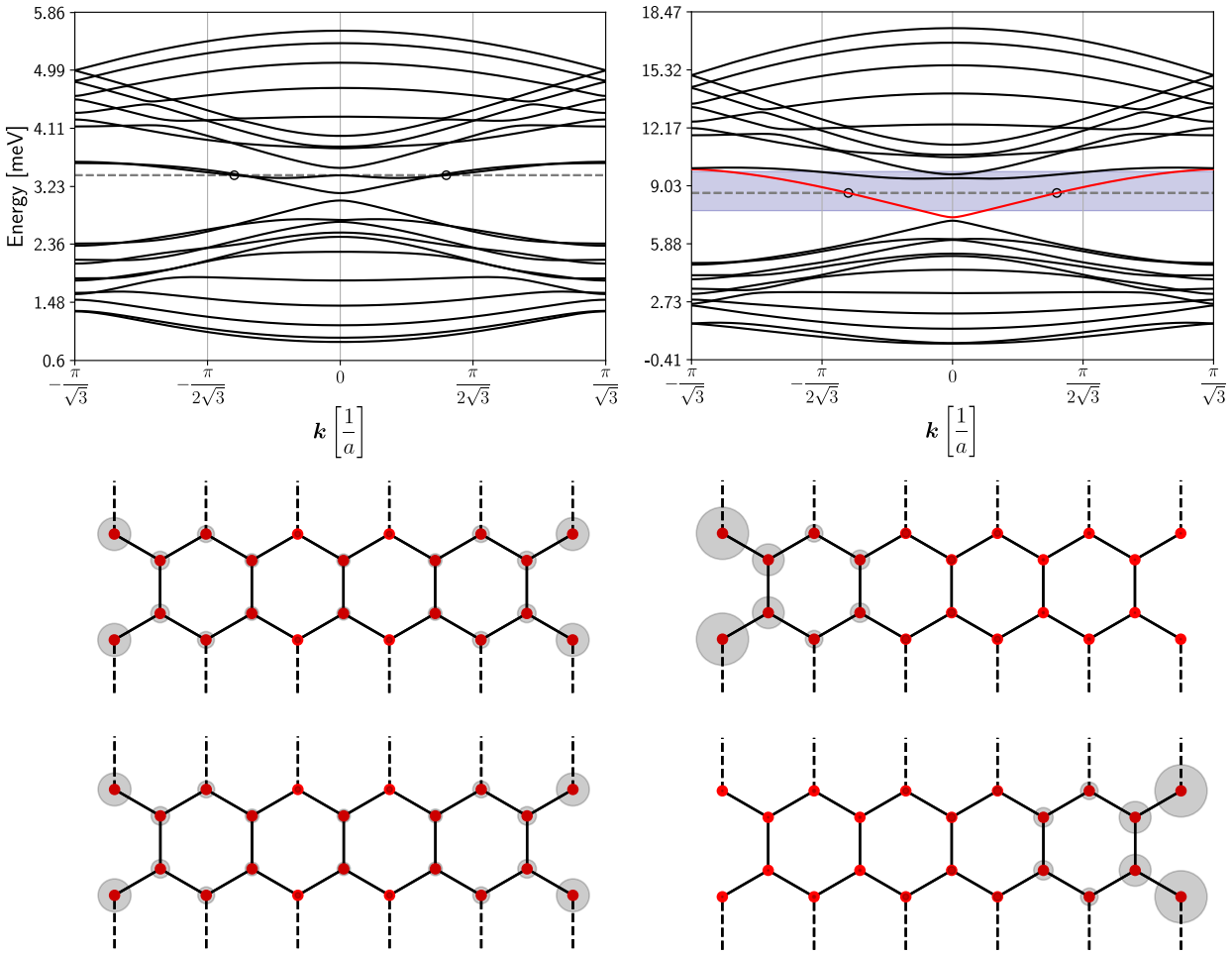

Figure 2.10: Dispersion relation and states corresponding to the marked energies for the armchair nanoribbon. **Left Panel:** Situation with $K = 0$. There is a resemblance with graphene, where two of the top bands lower their energies due to the on-site energy discrepancy at the edge. The plots below represent the magnitude of the probabilities for the two possible states with $E = 3.40$meV. The probability is proportional to the radii of the grey circles. **Right Panel:** Situation with $K = 4.07$meV. Bands preserve their basic structure and the two central bands are separated. The light-blue colored area is the gap of the bulk, which shows which band should have a topological behavior. The lower plots represent the probability of the states with $E = 8.64$meV. There is a clear localization at both edges of the ribbon.

From figures 2.8 and 2.10, we see that the states corresponding to the energies that cross between bands effectively are located in the border of the nanoribbon. This is a bigger hint that we are dealing with topologically protected states, but we still have to find a topological invariant to claim that the states of the Hamiltonian are topologically protected. To achieve this, we will start by analyzing the time reversal symmetry (TRS) of equation 2.14. Just as with topological tight-binding models, a broken TRS might give non trivial values of the Chern number. By finding that TRS is broken for the magnonic Hamiltonian, we will proceed to calculate the Chern number of our model with the care that we are dealing with bosons and not fermions.

2.4 Time Reversal Symmetry

In Quantum Mechanics, the time reversal operator is defined as $\mathcal{T} = UK$. Where U is a unitary operator and K is complex conjugation. A Hamiltonian has TRS if $\mathcal{T}H(q)\mathcal{T}^\dagger = H(q)$. To prove this, it must be noted that $\mathcal{T}\boldsymbol{S_{ij}}\mathcal{T}^\dagger = -\boldsymbol{S_{ij}}$. This implies that performing time reversal symmetry es equivalent to change the quantization axis from $\boldsymbol{z}$ to $-\boldsymbol{z}$. So we just have to rotate our axis around the $\boldsymbol{x}$ axis, which implies that Holstein-Primakoff's transformations are of the form:

$$S_{ia}^{(x)} = \sqrt{\frac{S}{2}}\left(a_i^\dagger + a_i\right) \qquad S_{ib}^{(x)} = \sqrt{\frac{S}{2}}\left(b_i^\dagger + b_i\right) \tag{2.19a}$$

$$S_{ia}^{(y)} = -\mathrm{i}\sqrt{\frac{S}{2}}\left(a_i^\dagger - a_i\right) \qquad S_{ib}^{(y)} = -\mathrm{i}\sqrt{\frac{S}{2}}\left(b_i^\dagger - b_i\right) \tag{2.19b}$$

$$S_{ia}^{(z)} = -S + a_i^\dagger a_i \qquad S_{ib}^{(z)} = -S + b_i^\dagger b_i \tag{2.19c}$$

Replacing this transformation into equation 2.6 leads to the complex conjugation of the coefficients in equation 2.14, which mathematically means that after applying time reversal symmetry the Hamiltonian is:

$$\begin{aligned}\mathcal{T}\mathcal{H}\mathcal{T}^\dagger = \frac{S}{2}\sum_{\boldsymbol{k},\boldsymbol{\delta}}\Bigg[&-\left(\mathcal{J}_{\boldsymbol{\delta}}^{xx} + \mathcal{J}_{\boldsymbol{\delta}}^{yy}\right)\left(e^{\mathrm{i}\boldsymbol{k}\cdot\boldsymbol{\delta}}a_{\boldsymbol{k}}^\dagger b_{\boldsymbol{k}} + e^{-\mathrm{i}\boldsymbol{k}\cdot\boldsymbol{\delta}}b_{\boldsymbol{k}}^\dagger a_{\boldsymbol{k}}\right)\\ &-\left(\mathcal{J}_{\boldsymbol{\delta}}^{xx} - \mathcal{J}_{\boldsymbol{\delta}}^{yy} + 2\mathrm{i}\mathcal{J}_{\boldsymbol{\delta}}^{xy}\right)e^{-\mathrm{i}\boldsymbol{k}\cdot\boldsymbol{\delta}}a_{\boldsymbol{k}}b_{-\boldsymbol{k}} - \left(\mathcal{J}_{\boldsymbol{\delta}}^{xx} - \mathcal{J}_{\boldsymbol{\delta}}^{yy} - 2\mathrm{i}\mathcal{J}_{\boldsymbol{\delta}}^{xy}\right)e^{\mathrm{i}\boldsymbol{k}\cdot\boldsymbol{\delta}}b_{-\boldsymbol{k}}^\dagger a_{\boldsymbol{k}}^\dagger\\ &+2\mathcal{J}_{\boldsymbol{\delta}}^{zz}\left(a_{\boldsymbol{k}}^\dagger a_{\boldsymbol{k}} + b_{\boldsymbol{k}}^\dagger b_{\boldsymbol{k}}\right)\Bigg] + 2AS\sum_{\boldsymbol{k}}\left(a_{\boldsymbol{k}}^\dagger a_{\boldsymbol{k}} + b_{\boldsymbol{k}}^\dagger b_{\boldsymbol{k}}\right)\end{aligned} \tag{2.20}$$

From equation 2.20 it is clear that we will only have that $\mathcal{T}\mathcal{H}\mathcal{T}^\dagger = \mathcal{H}$ when $J_{\boldsymbol{\delta}}^{xy} = 0$, which in the case of the model we have been describing we have that that condition is met only when $K = 0$. With this, we conclude that Kitaev's parameter breaks TRS and it is worth calculating the Chern number because it might have a non-trivial value.

2.5 Chern Number

The Chern number of the j-th energy band is [22, 23]

$$C_j = \frac{1}{2\pi}\int_{BZ}\mathrm{i}\epsilon_{\mu\nu}\ \mathrm{Tr}\Big[\left(1 - P_j\right)\left(\partial_{k_\mu}P_j\right)\left(\partial_{k_\nu}P_j\right)\Big]\mathrm{d}k^2\ , \tag{2.21}$$

where the integrand used to obtain the Chern number is called the Berry curvature and the operators P_j are the projection operators, which are defined as:

$$P_j = T_{\boldsymbol{k}}\Gamma_j\sigma_3 T_{\boldsymbol{k}}^\dagger\sigma_3\ . \tag{2.22}$$

Where $T_{\boldsymbol{k}}$ is the transformation matrix obtained from Colpa's algorithm, σ_3 is the paraunitary matrix and Γ_j is a $(2N, 2N)$ matrix with every element equal to 0, except for the j-th diagonal component that is equal to 1.

Ploting the values of the Berry curvature for two different and big K in the same path in $\boldsymbol{k}$-space used for the dispersion relation of the bulk, figure 2.11 is obtained. In the left panel we see the values for $K = 2.03$meV and in the right panel the case with $K = 4.07$, and in both cases the Berry curvature for the lower band is plotted in blue and for the top band in orange.

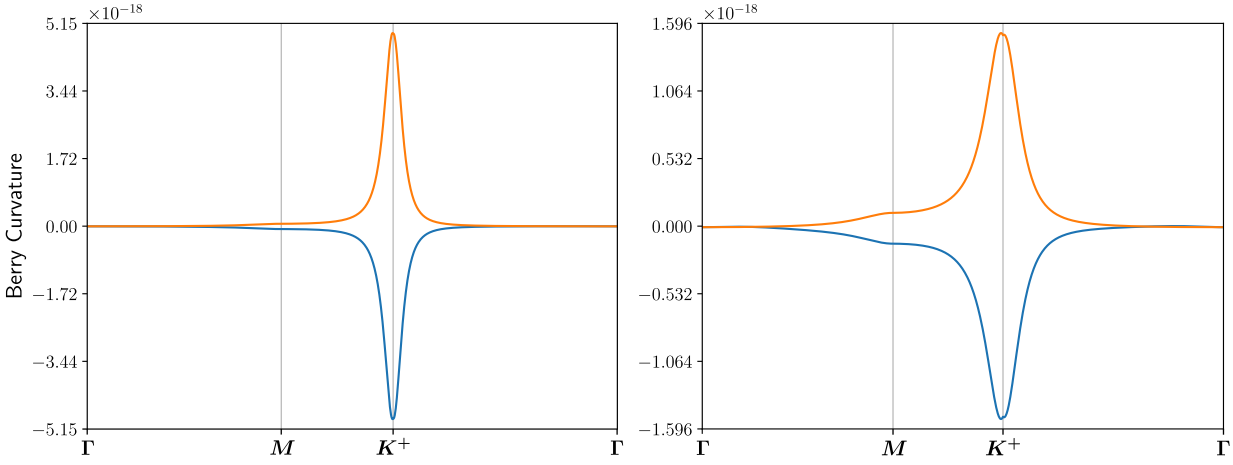

Figure 2.11: Berry curvature for CrI_3 given by the integrand of equation 2.21. In the left panel it can be seen the case with $K = 2.03$meV and in the right panel the case with $K = 4.07$meV. The importance of this plot relies on noticing that the case with lower value of K has a steeper maximum, which eventually diverges when $K \to 0$. The behavior seen at $\boldsymbol{K}^+$ in this plot can also be observed at $\boldsymbol{K}^-$.

From figure 2.11 it is important to acknowledge two important aspects. First, for lower values of K, the curve loses its smoothnes and eventually, for $K = 0$ it cannot be correctly defined as it was introduced in equation 2.21 because there is a degeneracy in the eigenenergies. The second important aspect is that for the same value of K, the shape of the curves for both energy levels is the same, but with opposite signs.

Integrating the Berry curvature in the first Brillouin zone, the actual Chern numbers are obtained. The lower band has Chern number $C_1 = -1$, while the upper band has $C_2 = 1$. The Chern must comply with the summation rule: For a Hamiltonian with $2N$ bands, we must have that sum of the first N Chern numbers must be zero $\left(\sum_j^N C_j = 0\right)$ [23]. The values obtained for the Chern of each band sum zero, so no errors are expected on this calculation.

It is also important to note that the value of the Chern numbers do not change of sign when K passes from a positive value to a negative one. This is because the chirality has already been defined, when the quantization axis $\boldsymbol{z}$ was chosen. To change the sign of the Chern number (i.e. obtain $C_1 = 1$) the quantization axis must be reversed in the same way as it was done for the analysis of the TRS.

2.6 Thermal Hall Effect

To finalize this chapter, we will study the thermal Hall effect in the presented model. In the context of bidimensional materials, it is common to study the great variety of Hall effects [24], where a potential difference in one direction implies the generation of an electric current in the perpendicular direction. When studying this effect in the particular case of topological insulators, it has been seen that the topological invariant is related to the existence of a quantum Hall state, where we can see as an example than in Haldane's model for graphene, the Hall conductivity in the topological state is [15]

$$\sigma_{xy} = \frac{e^2}{h} \ . \tag{2.23}$$

As magnons do not have electric charge, we cannot study the Hall effects usually studied in topological insulators. In this case, it is well-known that magnons contribute to the thermal currents that are produced in the existence of a thermal gradient [25]

$$T(\boldsymbol{r}) = T_0\big(1 - \chi(\boldsymbol{r})\big) \ , \tag{2.24}$$

where $\chi(\boldsymbol{r})$ is a parameter that describes the temperature's space-dependence. In the small gradient limit, it can be shown through linear response theory [] that the thermal current produced the thermal gradient is

$$\langle J_\mu \rangle = L^{\mu\nu}\left(T\partial_\nu\left(\frac{1}{T}\right) - \partial_\nu\chi\right) \ , \tag{2.25}$$

where $L^{\mu\nu}$ are the thermal transport coefficients, which can be used to express the thermal conductivity as

$$\kappa^{\mu\nu} = \frac{L^{\mu\nu}}{T} \ . \tag{2.26}$$

In reference [25] it is proven that in the particular case of non-interacting magnons, the thermal hall conductivity reads

$$\kappa^{xy}(T) = \frac{k_B^2 T}{(2\pi)^2\hbar}\sum_j \int_{BZ} c_2(n_B(\epsilon_{j\boldsymbol{k}}))\Omega_{j\boldsymbol{k}}\mathrm{d}k^2 \ . \tag{2.27}$$

Where the index i runs over the $m = 2$ energy levels, $\epsilon_{i\boldsymbol{k}}$ is the eigenenergy for the momentum $\boldsymbol{k}$, $\Omega_{i\boldsymbol{k}}$ is the Berry curvature given by the integrand of equation 2.21, n_B is the Bose distribution and c_2 is:

$$c_2(x) = (1+x)\left(\log\left(\frac{1+x}{x}\right)\right)^2 - \left(\log x\right)^2 - 2\mathrm{Li}_2(-x) \ , \tag{2.28}$$

$\mathrm{Li}_n(z)$ being the polylogarithm.

In figure 2.12 it is plotted the thermal Hall conductivity by direct numerical calculation of equation 2.27 for multiple values of the Kitaev parameter K. From the figure, it is

important to note that for the different values of K, the thermal Hall conductivity changes at different temperatures, making this effect a strong predictor that the Heisenberg-Kitaev model describes CrI_3. From the values of K that could be used, it should be pointed out that for $K = 4.07$meV, the conductivity changes of sign at $T = 7.51$K.

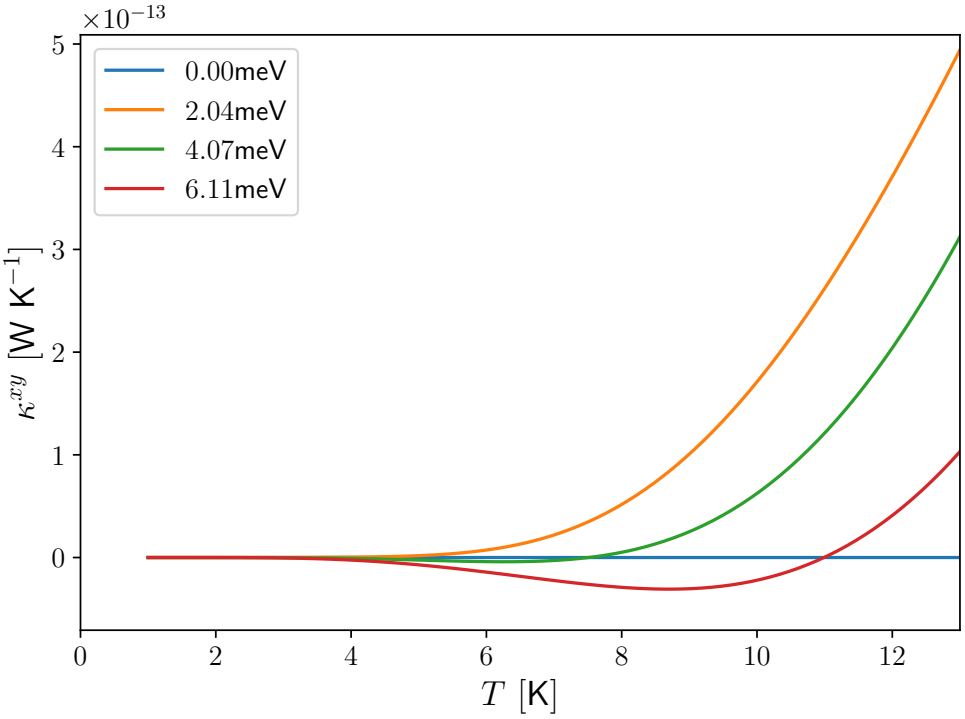

Figure 2.12: Thermal Hall conductivity as given by equation 2.27 for different values of K. For different values of K, the thermal Hall conductivity changes of sign at different temperatures.

2.7 Conclusion

In this section, a monolayer of CrI_3 was studied through the Heisenberg-Kitaev model of ferromagnets. It was numerically demonstrated that a gap opens between the two bands present in the dispersion relation when Kitaev's parameter is turned on. It was later proved that the nanoribbon possesses chiral edge states for the energies inside the bulk's energy gap for both zigzag and armchair borders, which is a strong sign of topological properties. Finally, it was shown that time-reversal symmetry is broken in the system due to Kitaev's parameter to ultimately show that the Chern number is non-trivial in CrI_3 with a nonzero Kitaev's parameter.

The idea that a Kitaev's parameter produces states with non-trivial topology turns most interesting when comparing it to previous publications, where signatures of topological magnons [17] were used to show that a nearest-neighbor DMI should describe bidimensional CrI_3. As it was constructively shown, this is not necessarily true due to the topological properties predicted through the Heisenberg-Kitaev model, and more experimental results are required to obtain the actual Hamiltonian of the bidimensional material. Because of this

last argument is that the calculation of the thermal Hall conductivity is crucial, as it provides as an outstanding signature of the Heisenberg-Kitaev model.

Chapter 3

Magnon Polarons in a Magnetic Field Gradient

The focus of this chapter is the study of Magnon polarons. These quasiparticles form due to the interaction between magnons and phonons [26]. These are usually studied by incorporating, to the magnon and phonon Hamiltonians, a phenomenological coupling [27], where there is no possibility of controlling the coupling because it is an intrinsic property of the material. The primary motivation for this chapter will be to study how a magnon-phonon interaction can be induced and ultimately controlled. For this, the formalism of phonons will be introduced in the simple case of a unidimensional lattice and later, generalize the study to an arbitrary lattice.

After the introduction of phonons, a Hamiltonian of a system with elastic and spin interactions will be presented. From this, it will be shown that a space-dependent magnetic field can generate magnon polarons. The main interest is to compare and contrast the properties of the coupling induced by the magnetic field with the phenomenological coupling that is usually studied.

3.1 Phonons in a Lattice

The simplest model where phonons can be studied is a unidimensional lattice, where each site has mass M and is coupled to its nearest-neighbor through springs with natural frequency ω_0 and natural length a. To further simplify the problem, it will assume that each site can only move in the longitudinal direction, as shown in figure 3.1.

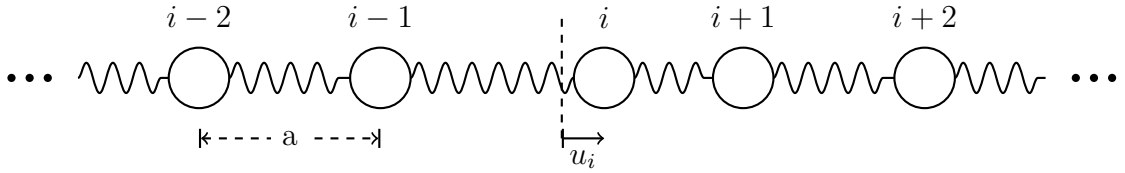

Figure 3.1: Unidimensional lattice with elastic coupling.

With all the mentioned considerations in mind, and using u_i to denote the displacement of each atom from its equilibrium position, the Hamiltonian that describes this system is:

$$\mathcal{H} = \sum_i \left[\frac{{p_i}^2}{2M} + \frac{M{\omega_0}^2}{2}\big(u_{i+1} - u_i\big)^2 \right] . \tag{3.1}$$

As previously stated, the main interest of this system is the study of its phonons. This study will be accomplished by transforming Hamiltonian 3.1 into a form, in terms of bosonic annihilation and creation operators c. For this, the variables p_i and x_i, are expressed in k-space through the discrete fourier transform:

$$x_i = \frac{1}{\sqrt{N}} \sum_k x_k e^{\mathrm{i}kia} , \tag{3.2a}$$

$$p_i = \frac{1}{\sqrt{N}} \sum_k p_k e^{\mathrm{i}kia} . \tag{3.2b}$$

Replacing the previous expression into Hamiltonian 3.1 gives us the Hamiltonian in k-space, which reads

$$\mathcal{H} = \sum_k \left[\frac{p_k p_{-k}}{2M} + M{\omega_0}^2\big(1 - \cos(ka)\big)u_k u_{-k} \right] . \tag{3.3}$$

We can now express the operators p_k and u_k in terms of annihilation and creation operators c_k and $c^\dagger_{-k}$ as [28]:

$$x_k = \sqrt{\frac{\hbar}{2M\omega_k}}\left(c^\dagger_{-k} + c_k\right) , \tag{3.4a}$$

$$p_k = \mathrm{i}\sqrt{\frac{\hbar M\omega_k}{2}}\left(c^\dagger_{-k} - c_k\right) , \tag{3.4b}$$

where,

$$\omega_k = \omega_0\sqrt{2 - 2\cos(ka)} = 2\omega_0\left|\sin\left(\frac{ka}{2}\right)\right| . \tag{3.5}$$

Replacing the previous transformation into Hamiltonian 3.3, the Hamiltonian of phonons for the unidimensional lattice is:

$$\mathcal{H} = \sum_k 2\hbar\omega_0\left|\sin\left(\frac{ka}{2}\right)\right|\left(c^\dagger_k c_k + \frac{1}{2}\right) . \tag{3.6}$$

It is worthy to note that because Hamiltonian 3.6 is already diagonalized, the dispersion relation is just equation 3.5, which is plotted in figure 3.2. From continuum mechanics, it's a well-known fact that acoustic sound waves have linear dispersion relations: $\Omega_k = v|k|$, where

v is the speed of sound. From equation 3.5, it is clear that in the long-wavelength limit (small k), the dispersion relation is $\omega_k = \omega_0 a|k|$. To have an accurate classical limit of the model, the sound velocity must be $v = \omega_0 a$. This fact will be used later to find the elastic constants from the nearest-neighbor distance a and sound speeds v.

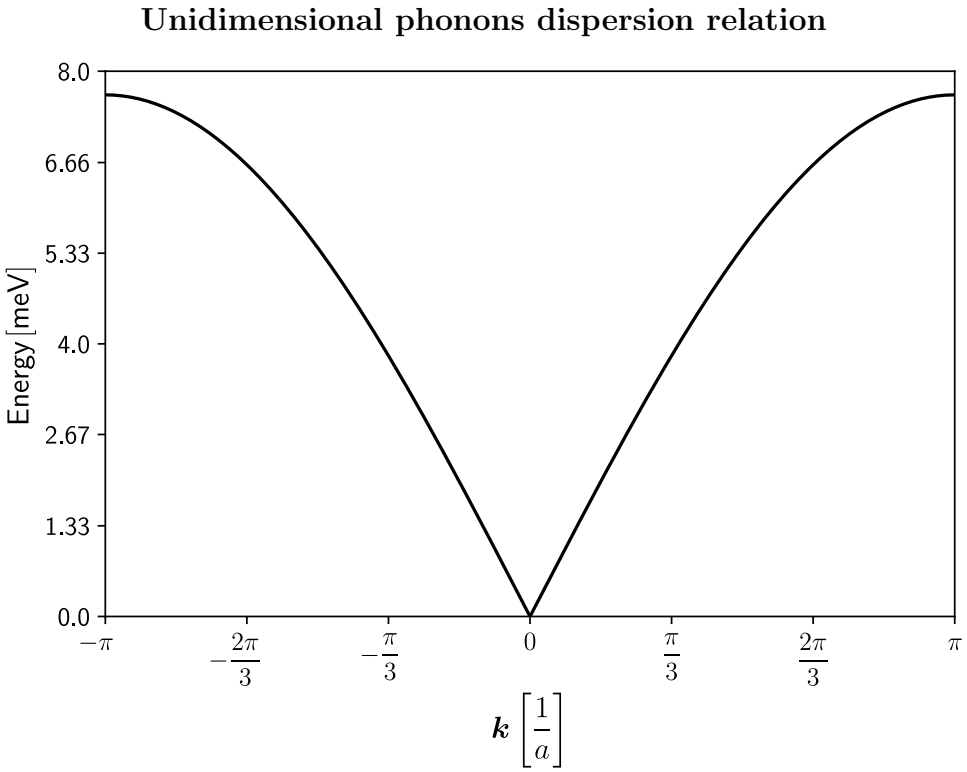

Figure 3.2: Dispersion relation for the unidimensional lattice of longitudinal phonons who's analytical expression is given by equation 3.5. The known values of YIG [26] have been used: $v_{\parallel} = 7209\text{ms}^{-1}$, $a = 1.24\text{nm}$ and $M = 9.810^{-24}\text{kg}$.

A central weakness of the introduced model is that only longitudinal phonons exist. To include transversal phonons, Hamiltonian 3.1 can be extended to allow displacements in the three spatial dimensions. This means that the Hamiltonian can be rewritten as

$$\mathcal{H} = \sum_i \left[\frac{\boldsymbol{p}_i^{\,2}}{2M} + \frac{1}{2}\left(u_{i+1}^{\alpha} - u_i^{\alpha}\right)\Phi^{\alpha\beta}\left(u_{i+1}^{\beta} - u_i^{\beta}\right) \right] , \tag{3.7}$$

where the elastic constant $M\omega_0^2$ has been replaced with the elastic tensor $\Phi^{\alpha\beta}$, which will allow us to work with the three spatial displacements and later in this section we will show how this parameter can be adjusted to fit the longitudinal and transversal sound speeds to have a good enough approximation of the material been studied.

To obtain the Hamiltonian that describe phonons we will develop a similar method to the one introduced for the purely unidimensional model. To express the position and momentum operators in k-space, we must first note that $\Phi^{\alpha\beta}$ must be real and symmetric as this tensor is theoretically obtained from the second order series expansion of the interaction potential

$V(u_{i+1}^{\alpha} - u_i^{\alpha})$ between two neighboring sites [28]. This implies that $\Phi^{\alpha\beta}$ is diagonalizable

$$\Phi^{\alpha\beta}\epsilon_{\lambda}^{\beta} = \phi_{\lambda}\epsilon_{\lambda}^{\alpha} \ , \tag{3.8}$$

with $\lambda = \{0, 1, 2\}$ eigenvalues and eigenvectors. This fact allows us to express $\boldsymbol{x}_i$ and $\boldsymbol{p}_i$ in k-space space as:

$$x_i^{\alpha} = \frac{1}{\sqrt{N}} \sum_{k\lambda} x_{k\lambda}\epsilon_{k\lambda}^{\alpha} e^{\mathrm{i}kia} \tag{3.9a}$$

$$p_i^{\alpha} = \frac{1}{\sqrt{N}} \sum_{k\lambda} p_{k\lambda}\epsilon_{k\lambda}^{\alpha} e^{\mathrm{i}kia} \ . \tag{3.9b}$$

Replacing equation 3.9 into Hamiltonian 3.7 leads us to

$$\mathcal{H} = \sum_{k\lambda} \left[\frac{p_{k\lambda}p_{-k\lambda}}{2M} + \frac{\phi_{\lambda}}{2}\left(e^{\mathrm{i}ka} - 1\right)\left(e^{-\mathrm{i}ka} - 1\right) u_{k\lambda}u_{-k\lambda} \right] \ , \tag{3.10}$$

where the operators $x_{k\lambda}$ and $p_{k\lambda}$ can be expressed in terms of creation and annihilation operators as

$$x_k = \sqrt{\frac{\hbar}{2M\omega_{k\lambda}}}\left(c_{-k\lambda}^{\dagger} + c_{k\lambda}\right) \qquad\qquad p_k = \mathrm{i}\sqrt{\frac{\hbar M\omega_{k\lambda}}{2}}\left(c_{-k\lambda}^{\dagger} - c_{k\lambda}\right) \tag{3.11}$$

with,

$$\omega_{k\lambda} = \sqrt{\frac{\phi_{\lambda}}{m}}\sqrt{2 - 2\cos(ka)} = 2\sqrt{\frac{\phi_{\lambda}}{m}}\left|\sin\left(\frac{ka}{2}\right)\right| \ , \tag{3.12}$$

to obtain the Hamiltonian for phonons

$$\mathcal{H} = \sum_{k\lambda} 2\hbar\sqrt{\frac{\phi_{\lambda}}{m}}\left|\sin\left(\frac{ka}{2}\right)\right|\left(c_{k\lambda}^{\dagger}c_{k\lambda} + \frac{1}{2}\right) \ . \tag{3.13}$$

As a first approximation, the values of $\Phi^{\alpha\beta}$ will be chosen in such a way that the dispersion relations given by equation 3.12 correctly reproduce the dispersion relation in the long-wavelength limit, which is known to be

$$\omega_{\lambda k} = c_{\lambda}\left|k\right| \ . \tag{3.14}$$

As an example, we can note that a material whose waves are classically described by a transversal sound speed of $v_{\perp}$ and a longitudinal sound speed of $v_{\parallel}$ is obtained from the following tensor:

$$\Phi^{\alpha\beta} = \frac{M}{a^2}\begin{pmatrix} {v_{\parallel}}^2 & 0 & 0 \\ 0 & {v_{\perp}}^2 & 0 \\ 0 & 0 & {v_{\perp}}^2 \end{pmatrix} \ . \tag{3.15}$$

In figure 3.3 we can see the dispersion relation of our model. Where we have used the values reported for YIG [26], which are $v_{\parallel} = 7209\text{ms}^{-1}$, $v_{\perp} = 3843\text{ms}^{-1}$, $M = 9.8 \cdot 10^{24}\text{kg}$ and $a = 1.24\text{nm}$.

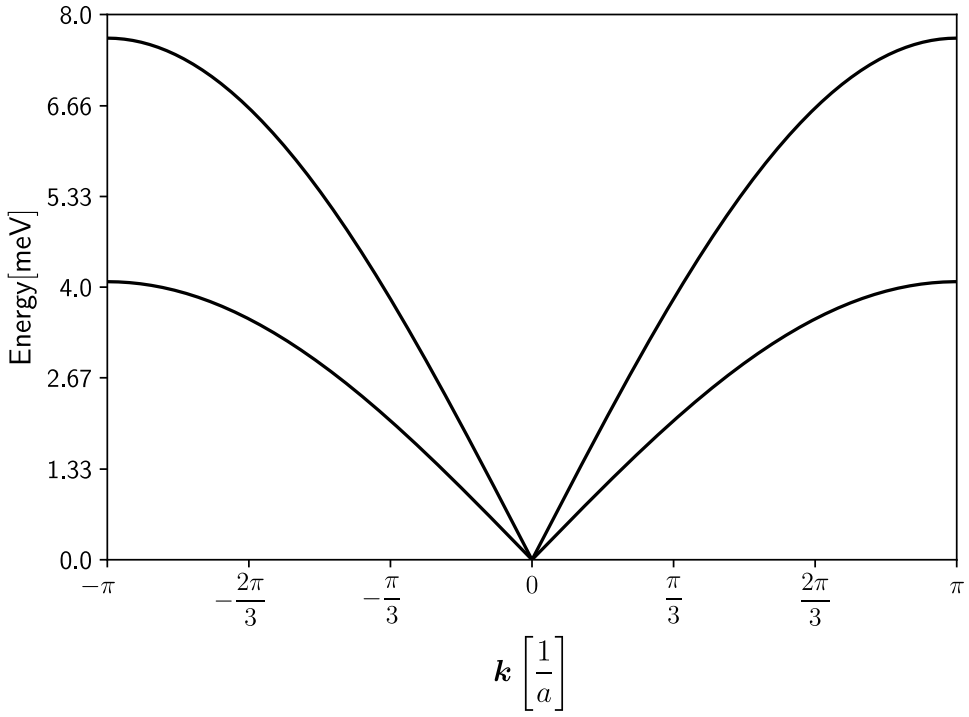

Figure 3.3: Dispersion relation for a unidimensional lattice with threedimensional phonons for the sound speeds of YIG. Its analytical expression is given by equation 3.12.

In this introduction on phonons, it was shown how transversal and longitudinal phonons appear naturally by considering a quadratic potential between sites. It was also explained how the parameters of Hamiltonian 3.7 can be fitted to correctly reproduce the long-wavelength limit.

To finish this introduction on phonons, we will study them in an arbitrary lattice. For this, we will drop the assumption that only nearest-neighbor exist, meaning that the Hamiltonian that describes the system becomes:

$$\mathcal{H} = \sum_{ij\alpha} \frac{{p_i^{j\alpha}}^2}{2M} + \sum_{ii'jj'} \frac{1}{2} u_i^{j\alpha} \Phi_{i-i'}^{j\alpha j'\beta} u_{i'}^{j'\beta} \ , \tag{3.16}$$

where we have that $i, i' \in \{0, 1, ..., N\}$ symbolizes the specific unit cell, $j, j' \in \{0, 1, ..., m-1\}$ is the specific site in the basis and $\alpha, \beta \in \{\hat{\boldsymbol{x}}, \hat{\boldsymbol{y}}, \hat{\boldsymbol{z}}\}$ are the three spatial coordinates. To obtain the Hamiltonian in $\boldsymbol{k}$-space we must start by using the following transformation:

$$\Phi_{i-i'}^{j\alpha j'\beta} = \sum_{\boldsymbol{k}} \Phi_{\boldsymbol{k}}^{j\alpha j'\beta} e^{\mathrm{i}\boldsymbol{k}\cdot(\boldsymbol{R}_i - \boldsymbol{R}_{i'})} \ , \tag{3.17}$$

where it is important to note that because $\Phi_{i-i'}^{j\alpha j'\beta}$ is real and symmetric, then $\Phi_{\boldsymbol{k}}^{j\alpha j'\beta}$ is also real and symmetric, which implies that it can be diagonalized as

$$\sum_{j'\beta} \Phi_{\boldsymbol{k}}^{j\alpha j'\beta} \epsilon_{\boldsymbol{k}\lambda}^{j'\beta} = \phi_{\boldsymbol{k}\lambda} \epsilon_{\boldsymbol{k}\lambda}^{j\alpha} \ , \tag{3.18}$$

with $\lambda \in 0, 1, ..., 3m-1$ eigenvalues and eigenvectors.

Now, we can continue with the same spirit as in the three-dimensional case and define the fourier trasnform of the position and momentum operators as

$$x_i^{j\alpha} = \frac{1}{\sqrt{N}} \sum_{\boldsymbol{k}\lambda} x_{\boldsymbol{k}\lambda} \epsilon_{\boldsymbol{k}\lambda}^{j\alpha} e^{\mathrm{i}\boldsymbol{k}\cdot\boldsymbol{R}_i} \tag{3.19a}$$

$$p_i^{j\alpha} = \frac{1}{\sqrt{N}} \sum_{\boldsymbol{k}\lambda} p_{\boldsymbol{k}\lambda} \epsilon_{\boldsymbol{k}\lambda}^{j\alpha} e^{\mathrm{i}\boldsymbol{k}\cdot\boldsymbol{R}_i} \ . \tag{3.19b}$$

and replace it into Hamiltonian 3.16 together with equation 3.17 to obtain that the Hamiltonian in $\boldsymbol{k}$-space reads

$$\mathcal{H} = \sum_{\boldsymbol{k}\lambda} \left[\frac{p_{\boldsymbol{k}\lambda} p_{-\boldsymbol{k}\lambda}}{2M} + \frac{\phi_{\boldsymbol{k}\lambda}}{2} u_{\boldsymbol{k}\lambda} u_{-\boldsymbol{k}\lambda} \right] \ . \tag{3.20}$$

All that remains is to write the position and momentum operators in term of creation and annihilation operators defined in the same way as in equation 3.11 to obtain

$$\mathcal{H} = \sum_{k\lambda} \hbar\omega_{k\lambda} \left(c_{k\lambda}^\dagger c_{k\lambda} + \frac{1}{2} \right) \ , \tag{3.21}$$

where the dispersion relation is

$$\omega_{k\lambda} = \sqrt{\frac{\phi_{k\lambda}}{M}} \ . \tag{3.22}$$

Numerically, it can be seen that the results of figure 3.3 are completely reproduced through the correct definition of the elastic tensor, which in this case reads

$$\Phi_{\boldsymbol{R}_i - \boldsymbol{R}_{i'}}^{\alpha\beta} = V^{\alpha\beta} \left(2\delta_{i,i'} - \delta_{i,i'+1} - \delta_{i,i'-1} \right) \ , \tag{3.23}$$

and can be transformed through equation 3.17 to obtain

$$\Phi_k^{\alpha\beta} = V^{\alpha\beta} \left(2 - e^{-\mathrm{i}ka} - e^{\mathrm{i}ka} \right) \ . \tag{3.24}$$

Where $V^{\alpha\beta}$ must have the same structure as $\Phi^{\alpha\beta}$ in equation 3.15.

The same analysis can be made more interesting by considering the same unidimensional lattice can be studied as if the base was described by two identical sites, a and b. In this case, the elastic tensor is

$$\Phi_{\boldsymbol{R}_i - \boldsymbol{R}_{i'}}^{j\alpha j'\beta} = V^{\alpha\beta} \left(2\delta_{i,i'}\delta_{j,j'} - \big(\delta_{i,i'} + \delta_{i,i'+1}\big)\delta_{j,0}\delta_{j',1} - \big(\delta_{i,i'} + \delta_{i,i'-1}\big)\delta_{j,1}\delta_{j',0} \right) \ , \tag{3.25}$$

which in $\boldsymbol{k}$-space reads

$$\Rightarrow \Phi_k^{j\alpha j'\beta} = V^{\alpha\beta}\left(2 - \left(1 + e^{-\mathrm{i}2ka}\right)\delta_{j,0}\delta_{j',1} - \left(1 + e^{\mathrm{i}2ka}\right)\delta_{j,1}\delta_{j',0}\right) . \tag{3.26}$$

In figure 3.4, it is shown the dispersion relation obtained with the elastic tensor given in equation 3.26. In this plot, it can be appreciated that there is no energy gap between the acoustic and optical bands, which is a direct consequence of the fact that both sites are identical. If there were to have different masses, an energy gap would appear, as shown in reference [29].

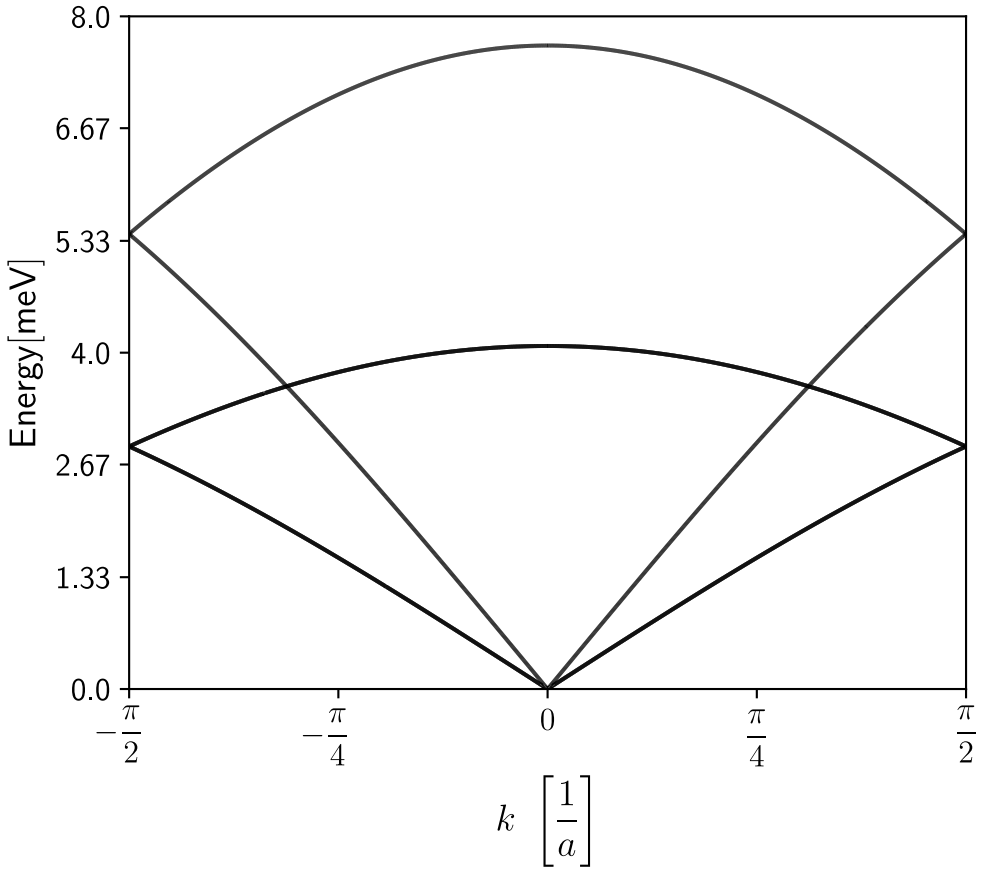

Figure 3.4: Dispersion relation for a unidimensional lattice with two identical sites. It was considered an elastic tensor given by equation 3.26 and energies written as in equation 3.22.

With this introduction of phonons, the theoretical floor to study the appearance of a magnon-phonon coupling from a space-varying magnetic field has been presented. But before examining this topic in depth, it must be noted that a magnetic field gradient induces forces to the system, so the equilibria of this system may vary. Recalling that in Holstein-Primakoff it was assumed that the classical equilibrium is $\boldsymbol{S} = (0, 0, S)$ is an equilibrium, and in the phonon quantization the stable equilibrium is $\boldsymbol{u} = (0, 0, 0)$, it is essential to show that classically, both equilibria are still stable after incorporating the magnetic field gradient. In the next section, the stability of a system composed of a single spin in a quadratic potential and a space-varying magnetic field will be studied.

3.2 Equilibrium in a Space-Varying Magnetic Field

Up to now, the Hamiltonian for phonons and magnons were obtained separately. Before proceeding onto studying the coupling between both quasiparticles, it is essential to analyze the classical equilibrium of the system. This study is crucial because a magnetic field gradient creates a force on every magnetic dipole, which could change the behavior of its equilibria. The equilibria will be studied in a system composed of a single spin attached to a spring to generate in a space-varying magnetic field. The presented toy model will be used to create a strong intuition so that the later equilibria analysis in the unidimensional lattice appears more natural.

The analysis of equilibria will be done by considering a system composed of a single spin attached to a spring and coupled to a magnetic field gradient, which is described by:

$$\mathcal{H} = \frac{\boldsymbol{p}^2}{2M} + \frac{m{\omega_0}^2}{2}\boldsymbol{u}^2 - \mu_B g \boldsymbol{B}\cdot\boldsymbol{S}\ . \tag{3.27}$$

Classically, the spin's time evolution is governed by Newton's second law and Landau-Lifschitz-Gilbert equation. To make the study of system's equilibria more comfortable, the spin variable can be written in spherical coordinates angles θ, ϕ and, it can be considered the particular case where $\boldsymbol{B} = (B^x(x), 0, B^z)$, meaning that the Hamiltonian is given by:

$$\mathcal{H} = \frac{\boldsymbol{p}^2}{2M} + \frac{M{\omega_0}^2}{2}\boldsymbol{u}^2 - \mu_B g S B^x \sin(\theta)\cos(\phi) - \mu_B g S B^z \cos(\theta)\ . \tag{3.28}$$

From equation 3.28, the equilibria of the system by minimizing the energy. For this, it must be imposed that $\partial_x E = 0$, $\partial_\theta E = 0$ and $\partial_\phi E = 0$:

$$M{\omega_0}^2 x - \mu_B g S \frac{\partial B^x}{\partial x}\sin(\theta)\cos(\phi) = 0 \tag{3.29a}$$

$$B^x\cos(\theta)\cos(\phi) - B^z\sin(\theta) = 0 \tag{3.29b}$$

$$B^x\sin(\theta)\sin(\phi) = 0\ . \tag{3.29c}$$

From equation 3.29, it is direct to see that $(x, \theta, \phi) = (0, 0, 0)$ is a solution. Studying the Hessian at the equilibrium point, it is clear that this is positive definite whenever the following inequality complies:

$$\left(\left.\frac{\partial B^x}{\partial x}\right|_{x=0}\right)^2 < \frac{M\omega_0^2}{g\mu_B S}B^z \tag{3.30}$$

Thus, the point $(x, \theta, \phi) = (0, 0, 0)$ is a stable equilibrium whenever the condition established by inequality 3.30 is fulfilled. The importance of analyzing the equilibrium of Hamiltonian 3.27 comes from the fact that the equilibrium needs to be stable for it to have spin waves. This toy model allows us to see that there exists a magnetic field gradient from which the equilibrium is no longer stable.

The most simple system with both magnetic and elastic interaction is given by:

$$\mathcal{H} = \sum_i \left[\frac{\boldsymbol{p}_i{}^2}{2M} + \frac{m{\omega_0}^2}{2}(\boldsymbol{u}_{i+1} - \boldsymbol{u}_i)^2 - J\boldsymbol{S}_i \cdot \boldsymbol{S}_{i+1} - \mu_B g \boldsymbol{B} \cdot \boldsymbol{S}_i \right] , \tag{3.31}$$

where the unidimensional elastic interaction and Heisenberg exchange were considered. To further simplify the model, the magnetic field $\boldsymbol{B}(x)$ will be assumed to be periodic with a periodicity equal to that of the lattice.

Expanding to first order the arbitrary magnetic field $\boldsymbol{B}(x)$ around the equilibrium positions $\boldsymbol{x}_{0i}$, leads to:

$$\mathcal{H} = \sum_i \left[\frac{\boldsymbol{p}_i{}^2}{2M} + \frac{m{\omega_0}^2}{2}(\boldsymbol{u}_{i+1} - \boldsymbol{u}_i)^2 - J\boldsymbol{S}_i \cdot \boldsymbol{S}_{i+1} - \mu_B g \boldsymbol{B} \cdot \boldsymbol{S}_i - \mu_B g \frac{\partial \boldsymbol{B}}{\partial x^\mu} \cdot \boldsymbol{S}_i x^\mu \right] , \tag{3.32}$$

where the positions $\boldsymbol{x}_{0i} = (ia, 0, 0)$ and the spins $\boldsymbol{S}_{0i} = (0, 0, S)$ as possible equilibria of the system.

To study the equilibria of Hamiltonian 3.31, the spin variable will be written in term of its spherical angles θ_i and ϕ_i and, as in the single spin case, it will be assumed that the magnetic field is given by $\boldsymbol{B} = (B^x(x), 0, B^z)$. With these considerations, the Hamiltonian can be written explicitly as:

$$\begin{aligned} \mathcal{H} = \sum_i \Bigg[& \frac{\boldsymbol{p}_i{}^2}{2M} + \frac{m{\omega_0}^2}{2}(\boldsymbol{u}_{i+1} - \boldsymbol{u}_i)^2 - JS^2 \Big(\sin(\theta_i)\sin(\theta_{i+1})\cos(\phi_i)\cos(\phi_{i+1}) \\ & + \sin(\theta_i)\sin(\theta_{i+1})\sin(\phi_i)\sin(\phi_{i+1}) + \cos(\theta_i)\cos(\theta_{i+1}) \Big) \\ & - \mu_B g \Big(SB^x(x)\sin(\theta_i)\cos(\phi_i) + SB^z\cos(\theta_i) \Big) \Bigg] . \end{aligned} \tag{3.33}$$

Using the single spin case as inspiration, the point $(u_i, \theta_i, \phi_i) = (0, 0, 0)$ as possible equilibrium. Expanding Hamiltonian 3.33 to second order around the mentioned point:

$$\mathcal{H} = \sum_i \left[\frac{\boldsymbol{p}_i{}^2}{2M} + \frac{m{\omega_0}^2}{2}(\boldsymbol{u}_{i+1} - \boldsymbol{u}_i)^2 - JS^2 \Big(\theta_i\theta_{i+1} - \theta_i{}^2 - \theta_{i+1}{}^2 \Big) - \mu_B g \boldsymbol{B} \cdot \boldsymbol{S}_i \right] . \tag{3.34}$$

To find the stability of the system, Fourier's theorem on u_i and θ_i will be used. This will lead to a Hamiltonian described by u_k, u_{-k}, θ_k and θ_{-k}, which is given by:

$$\begin{aligned} \mathcal{H} = \sum_k \Bigg[& \frac{p_k{}^2}{2M} + m{\omega_0}^2 \Big(1 - \cos(ka) \Big) u_k u_{-k} - 2JS^2 \Big(1 - \cos(ka) \Big) \theta_k \theta_{-k} \\ & + \mu_B g S B^z \theta_k \theta_{-k} - \mu_B g S B' u_k \theta_{-k} \Bigg] , \end{aligned} \tag{3.35}$$

where

$$B' \equiv \left.\frac{\partial B^x}{\partial x}\right|_{x=0} . \tag{3.36}$$

From the Hamiltonian in k-space, it can be noted that the Hessian is a block diagonal matrix, where each block is 4×4, formed by the variables u_k, θ_k, u_{-k} and θ_{-k}. With this, it can be proved that every eigenvalue is positive if and only if

$$\Big(Sg\mu_B B'\Big)^2 < 4mS{\omega_0}^2\Big(-2JS\big(1-\cos(ak)\big)+\mu_B g B^z\Big)\sin^2\left(\frac{ak}{2}\right) . \tag{3.37}$$

From equation 3.37, it is essential to recall that stable equilibrium is obtained if every eigenvalue of the Hessian is positive. In this particular case it must be noted that there always exists a value of k such that the obtained expression is not satisfied. This means that the Holstein-Primakoff's transformation expressed in equation 1.14 will not yield stable magnons. As an extra note, it is essential to recognize that, intuitively, the proposed equilibrium could never be stable because every site feels the same force, thus always pushing it away from the equilibrium obtained with a constant magnetic field.

3.3 Magnon-Phonon Coupling

As it was proven analitically in the previous section, the problem with a space-varying magnetic field with the same periodicity of the lattice is always unstable, which intuitively makes sense. This problem can be sorted out by changing the periodicity of the magnetic field to ma, where $m \in \mathbb{N}$. This means that the originally unidimensional lattice has to be described by a superlattice with m distinct but identical sites. Mathematically, the Hamiltonian transforms to:

$$\mathcal{H} = \mathcal{H}^{(ph)} + \mathcal{H}^{(m)} - \mu_B g \sum_{ij} {B'}_j^{\alpha\beta} S_i^{j\alpha} u_i^{j\beta} . \tag{3.38}$$

Where $H^{(ph)}$ and $H^{(m)}$ are described by equations 3.21 and 1.27 respectively. Additionally we have defined

$${B'}_j^{\alpha\beta} \equiv \left.\frac{\partial B^\alpha}{\partial r^\beta}\right|_{\boldsymbol{r}=\boldsymbol{R}_j} , \tag{3.39}$$

where $\boldsymbol{R}_j$ is the equilibrium position relative to the unit cell's origin.

From equation 3.38, the bosonic form of the third term, which is going to be called $\mathcal{H}^{(mp)}$, is the only one missing. The first step is to express the spins $\boldsymbol{S}_{ij}$ in terms of creation and annihilation operators employing equation 1.10, which leads to:

$$\mathcal{H}^{(mp)} = -\mu_B g\sqrt{\frac{S}{2}}\sum_{ij}\left[\Big({B'}_j^{x\beta} + i{B'}_j^{y\beta}\Big)u_{ij}^\beta a_{ij}^\dagger + \Big({B'}_j^{x\beta} - i{B'}_j^{y\beta}\Big)u_{ij}^\beta a_{ij}\right] . \tag{3.40}$$

Using the discrete Fourier series as presented in equations 1.18 and 3.11 we obtain

$$\mathcal{H}^{(mp)} = -\mu_B g\sqrt{\frac{S}{2}}\sum_{\boldsymbol{k}j\lambda}\left[\left(B'^{x\beta}_j + iB'^{y\beta}_j\right)\epsilon^{\beta}_{\boldsymbol{k}\lambda}u_{\boldsymbol{k}\lambda}a^{\dagger}_{\boldsymbol{k}j} + \left(B'^{x\beta}_j - iB'^{y\beta}_j\right)\epsilon^{\beta}_{\boldsymbol{k}\lambda}u_{\boldsymbol{k}\lambda}a_{-\boldsymbol{k}j}\right] . \quad (3.41)$$

Finally, by expressing $u_{\boldsymbol{k}\lambda}$ as creation and annihilation operators through equation 3.11 it is obtained that the magnon-phonon coupling Hamiltonian is:

$$\begin{aligned}\mathcal{H}^{(mp)} = -\mu_B g\sum_{\boldsymbol{k}j\lambda}\sqrt{\frac{S\hbar}{4M\omega_{\boldsymbol{k}\lambda}}}\Bigg[&\left(B'^{x\beta}_j + \mathfrak{i}B'^{y\beta}_j\right)\epsilon^{\beta}_{\boldsymbol{k}\lambda}\left(c_{\boldsymbol{k}\lambda} + c^{\dagger}_{-\boldsymbol{k}\lambda}\right)a^{\dagger}_{\boldsymbol{k}j} \\ &+ \left(B'^{x\beta}_j - \mathfrak{i}B'^{y\beta}_j\right)\epsilon^{\beta}_{\boldsymbol{k}\lambda}\left(c_{\boldsymbol{k}\lambda} + c^{\dagger}_{-\boldsymbol{k}\lambda}\right)a_{-\boldsymbol{k}j}\Bigg] . \end{aligned} \quad (3.42)$$

Now that the full Hamiltonian for magnons and phonons has been obtained, it is clear its resemblance with the coupling due to the phenomenological coupling [27]. The main difference between both mechanisms is that the coupling presented in this section can be controlled to obtain a coupling with any phonon by choosing the direction where the magnetic field varies, while Kittel's phenomenological coupling only couples the magnon with the transverse phonons [30]. As an example, under the influence of a field of the form $\boldsymbol{B}(x)$, only the longitudinal phonons will couple to the magnons, while a magnetic field of the form $\boldsymbol{B}(y,z)$ will couple the magnons to the transversal phonons.

Before continuing with the analysis of our system, we will make a brief parenthesis by comparing the analytical results of the previous section with the numerical results obtained through Colpa's algorithm. For this comparisson, we will consider the constants reported on YIG [26] shown in table 3.1, and a magnetic field is described by

$$\boldsymbol{B}(y) = B^y \sin\left(\frac{2\pi}{a}y\right)\hat{\boldsymbol{y}} + B^z\hat{\boldsymbol{z}} . \quad (3.43)$$

Parameter	Value
S	20
M	9.8×10^{-24} kg
a_0	12.376 Å
$v_{\parallel}$	7209 m/s
$v_{\perp}$	3843 m/s
J	0.24 meV

Table 3.1: Reported values of YIG.

What is interesting about this example, is that inequality 3.37 predicts the zone where Colpa's algorithm works correctly. This is shown in figure 3.5, where the vertical dotted line

corresponds to the value of k where the inequality begins to be satisfied. This line matches with the point where Colpa's algorithm begins to work because the quadratic form of the magnon-phonon Hamiltonian becomes definite possitive.

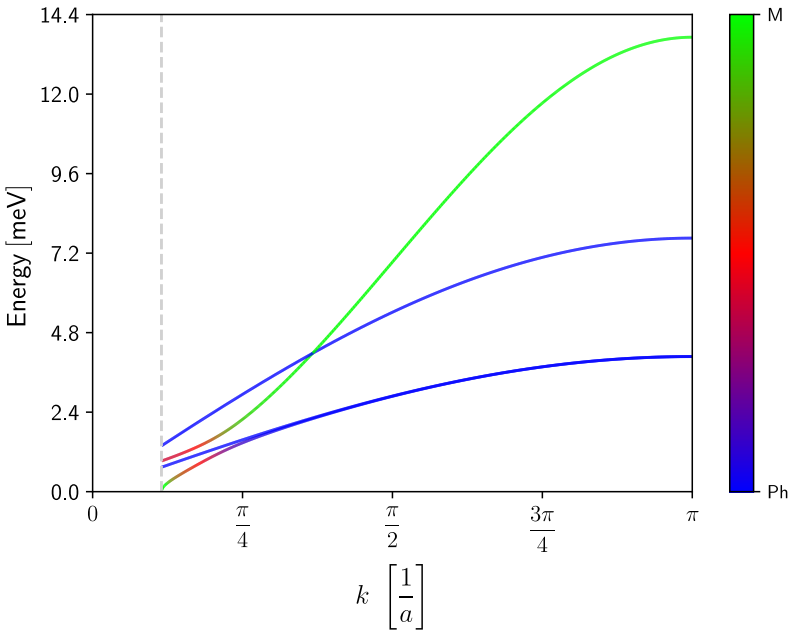

Figure 3.5: Magnon-Polarons' dispersion relation for a magnetic field with the same periodicity of the lattice. The colorbar is a measure of the probability that the corresponding eigenstate is a magnon, where a probability of zero means the band is phononic band (blue) and one is a magnonic band (green). The vertical dotted line corresponds to the theoretical prediction of the value of k upon which the inequality 3.37 is no longer satisfied, which coincides with the value from which the quadratic form of the Hamiltonian is no longer positive definite.

The principal importance of this brief parenthesis is that if Colpa's algorithm behaves appropriately in every possible value of k, then the equilibrium upon which the expansion of magnons and phonon was made is a stable equilibrium. It is also important to note that in this particular analysis, the point $k = 0$ will not be included as $\omega_{k\lambda}\big|_{k=0} = 0$, implying that the creation and annihilation operators are not correctly defined in that precise point due to a division over zero appearing in its definition given in equation 3.11.

Returning to the analysis of the magnon-phonon coupling, we are going to study a unidimensional lattice describes by the constants given in table 3.1 and a space-varying magnetic field that reads

$$\boldsymbol{B}(x,y) = B^x \sin\left(\frac{2\pi}{ma}x\right)\hat{\boldsymbol{x}} + B^y \sin\left(\frac{2\pi}{ma}y\right)\cos\left(\frac{2\pi}{ma}x\right)\hat{\boldsymbol{y}} + B^z\hat{\boldsymbol{z}}\ , \tag{3.44}$$

where it is important to note that it has a different periodicity of the lattice and in the case where $m \in \mathbb{N}$ there will be precisely m sites per unit-cell.

A completely stable system can be obtained in the case with $m = 2$, as it is shown in figure

3.6, where we have plotted the dispersion relations for different values of the magnetic field presented in equation 3.44. Here it is numerically shown that the coupling between magnons and the different phonon polarizations depends directly on the magnetic field gradients' direction. In the same figure, it can also be seen that magnons can couple to either acoustic or optical phonons.

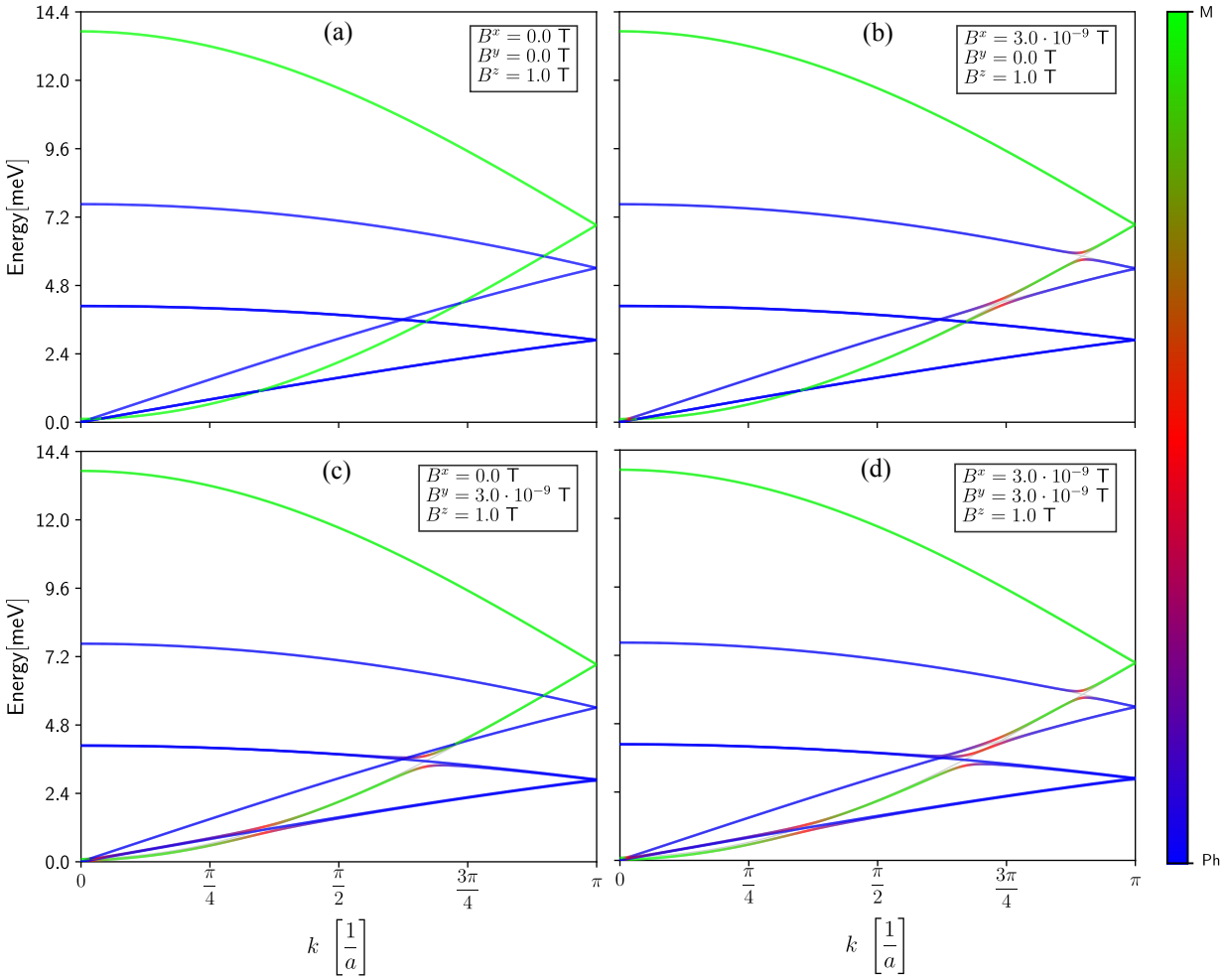

Figure 3.6: Dispersion relation obtained by diagonalizing the magnon-phonon Hamiltonian for the values given in table 3.1 and the magnetic field described by equation 3.44, for different values of B^x and B^y. The colorbar is the probability the corresponding eigenstate is a magnon. **(a)** Case with no magnetic field gradient, where the magnon and phonon bands are completely independent and no magnon polarons are seen. **(b)** Case where the magnetic field variation occurs in the $\hat{\boldsymbol{x}}$-direction, where magnon polarons (red) are generated in the anti-crossing points between the magnon and longitudinal phonon bands. **(c)** Case where the magnetic field variation occurs in the $\hat{\boldsymbol{y}}$-direction, where magnon polarons are generated in the anti-crossing points between the magnon and transversal phonon bands. **(d)** Case where the magnetic field variation occurs in the $\hat{\boldsymbol{x}}$ and $\hat{\boldsymbol{y}}$ directions. In this case magnon polarons are created in the anti-crossing points between magnons and the longitudinal and transversal phonon bands.

When studying figure 3.6.a in detail, it can be appreciated that there exist three crossing

points between the magnonic bands and the longitudinal phonons, and three additional ones for the transversal phonons bands. When the magnetic field gradient is turned on, the crossing points become anti-crossing points and a local energy gap can be measured. Performing this measurement for different magnetic field values of the magnetic field presented in equation 3.44, we obtain figure 3.7. In the left panel we see the case with variable B^x and $B^y = 0$, while in the the left panel we have $B^x = 0$ and variable B^y. In both cases we have plotted the gap at the values of k such that at zero magnetic field gradient the crossing point is found at that value of k, which correspond to three points in both cases. The most important aspect of this plots is that the energy gap depends linearly with respect to the magnetic field gradient.

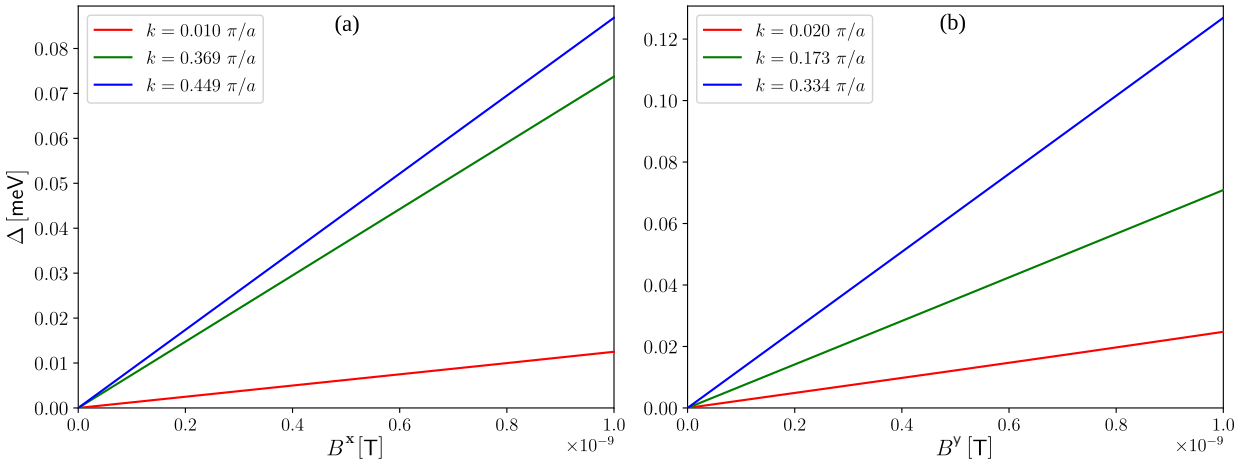

Figure 3.7: Energy gap for different values of the magnetic field presented in equation 3.44. In blue and orange, it is shown the gap in the two crossings between acoustic magnon and acoustic phonons, while in green, it is shown the gap between an acoustic magnon band with the optical band. **(a)** Coupling between magnons and the longitudinal phonons through a gradient in the $\hat{\boldsymbol{x}}$ direction, where we have fixed $B^y = 0$. **(b)** Coupling between magnons and the transversal phonons through a gradient in the $\hat{\boldsymbol{y}}$ direction, where we have fixed $B^x = 0$.

One fact that has been ignored until now, is that YIG actually has a nonzero phenomelogical magnetoelastic coupling. In previous works it can be seen that the energy gap for YIG is roughly $\Delta \approx 2.07\mu$eV[26]. This value can be used to compare the effectiveness of our model, where we have completely ignore the phenomelogical coupling. In table 3.2 we see what magnetic field and corresponding magnetic field gradient is needed to obtain the real gap found in YIG for the anti-crossing points produced due to the coupling between magnons and the longitudinal and transversal phonons. According to this results, it is needed an important magnetic field gradient, but achievable with the already available experimental techniques.

$\boldsymbol{k}$-Point	Magnetic field [T]	Gradient [T/m]
0.010 π/a_0	$B^x = 1.66 \cdot 10^{-10}$	0.421
0.369 π/a_0	$B^x = 2.81 \cdot 10^{-11}$	0.071
0.449 π/a_0	$B^x = 2.38 \cdot 10^{-11}$	0.060
0.020 π/a_0	$B^y = 8.49 \cdot 10^{-11}$	0.216
0.173 π/a_0	$B^y = 2.93 \cdot 10^{-11}$	0.074
0.334 π/a_0	$B^y = 1.63 \cdot 10^{-11}$	0.041

Table 3.2: For each of the crossing points, we show what magnetic field is needed to obtain a gap of 2.07μeV. The first three entries correspond to crossing points between magnons and longitudinal phonons, while the last three correspond to the crossing points between magnons and transversal phonons. The value of the magnetic field gradient is simply given by $\pi B^\mu/a$.

3.4 Conclusion

In this section, it was shown how magnons and phonons could couple through a space-varying magnetic field to obtain magnon polarons near the crossing points of between both bands in the absence of this coupling. In contrast to the usually used coupling generated by Kittel's phenomenological parameter, one of the most important features of the proposed coupling is that it is not material dependent in the sense that, in principle, the magnetic field shape could always be varied to obtain a desired coupling strength. The mentioned strength is also its weakness due to the difficulty of producing big enough magnetic field gradients for the effects to be measurable. Another outstanding feature the proposed coupling has to offer is that in theory, the coupling could be controlled to choose if the magnon would couple to the transverse or longitudinal phonon.

Chapter 4

Conclusion

In this thesis we studied magnons in collinear ferromagnets in two different systems. In the first system we showed that the topological magnons in monolayers of CrI_3, which were believed to come from a next-nearest-neighbor DMI, could also come from a nearest-neighbor Heisenberg-Kitaev model. The second system we studied the generation of magnon-phonon coupling through a space-varying magnetic field, where in the existing literature only the phenomenological magnetoelastic coupling has been studied.

In the second chapter of this thesis, where we studied monolayers of CrI_3 through the Heisenberg-Kitaev model it was numerically demonstrated that a non-zero Kitaev parameter opens an energy gap in the bulk's dispersion relation of the material. The energy gap and the similarity with the tight-binding models seen in topological insulators served as inspiration to study nanoribbons of CrI_3, where we found chiral edge-states. This lead us to study the time-reversal symmetry, which is broken due to the Kitaev parameter and ultimately gives rise to a non-trivial Chern number in the case with a nonzero Kitaev parameter. At the end of this chapter we showed that our model present thermal Hall effect, with the singularity that a change in the sign of the thermal Hall conducivity should exist when the temperature is lowered.

In the third chapter, we studied the magnetoleastic coupling produced by a space-varying magnetic field, where we obtained magnon polarons near the crossing points of between both bands in the absence of this coupling. In contrast to the magnetoelastic coupling generated by Kittel's phenomenological parameter, the proposed magnon-phonon coupling can be tuned by the control of the magnetic field's shape. This coupling also presents the advantage that the coupled phonon mode can be controlled by choosing the direction in which the magnetic field varies.

Bibliography

[1] Assa Auerbach. *Interacting electrons and quantum magnetism*. Springer Science & Business Media, 2012.

[2] Alexander Altland and Ben D Simons. *Condensed matter field theory*. Cambridge university press, 2010.

[3] Supriyo Bandyopadhyay and Marc Cahay. *Introduction to spintronics*. CRC press, 2015.

[4] M Lakshmanan. The fascinating world of the landau–lifshitz–gilbert equation: an overview. *Philosophical Transactions of the Royal Society A: Mathematical, Physical and Engineering Sciences*, 369(1939):1280–1300, 2011.

[5] T Holstein and Hl Primakoff. Field dependence of the intrinsic domain magnetization of a ferromagnet. *Physical Review*, 58(12):1098, 1940.

[6] Piers Coleman. *Introduction to many-body physics*. Cambridge University Press, 2015.

[7] GM Wysin. Quantization of the free electromagnetic field: Photons and operators. *Department of Physics, Kansas State University*, 2011.

[8] John W Negele. *Quantum many-particle systems*. CRC Press, 2018.

[9] Jun John Sakurai and Eugene D Commins. *Modern quantum mechanics, revised edition*. American Association of Physics Teachers, 1995.

[10] A Roldán-Molina, AS Nunez, and Joaquín Fernández-Rossier. Topological spin waves in the atomic-scale magnetic skyrmion crystal. *New Journal of Physics*, 18(4):045015, 2016.

[11] Alejandro Roldán-Molina. *Magnónica a Escala Atómica*. PhD thesis, Universidad de Chile, 2014.

[12] JHP Colpa. Diagonalization of the quadratic boson hamiltonian. *Physica A: Statistical Mechanics and its Applications*, 93(3-4):327–353, 1978.

[13] Gene H Golub and Charles F Van Loan. *Matrix computations*, volume 3. JHU press, 2012.

[14] Bevin Huang, Genevieve Clark, Efrén Navarro-Moratalla, Dahlia R Klein, Ran Cheng, Kyle L Seyler, Ding Zhong, Emma Schmidgall, Michael A McGuire, David H Cobden, et al. Layer-dependent ferromagnetism in a van der waals crystal down to the monolayer limit. *Nature*, 546(7657):270–273, 2017.

[15] F. Duncan M. Haldane. Model for a quantum hall effect without landau levels: Condensed-matter realization of the" parity anomaly". *Physical review letters*, 61(18):2015, 1988.

[16] Charles L Kane and Eugene J Mele. Quantum spin hall effect in graphene. *Physical review letters*, 95(22):226801, 2005.

[17] Lebing Chen, Jae-Ho Chung, Bin Gao, Tong Chen, Matthew B Stone, Alexander I Kolesnikov, Qingzhen Huang, and Pengcheng Dai. Topological spin excitations in honeycomb ferromagnet cri 3. *Physical Review X*, 8(4):041028, 2018.

[18] SA Owerre. A first theoretical realization of honeycomb topological magnon insulator. *Journal of Physics: Condensed Matter*, 28(38):386001, 2016.

[19] Changsong Xu, Junsheng Feng, Hongjun Xiang, and Laurent Bellaiche. Interplay between kitaev interaction and single ion anisotropy in ferromagnetic cri 3 and crgete 3 monolayers. *npj Computational Materials*, 4(1):1–6, 2018.

[20] AT Costa, DLR Santos, NMR Peres, and J Fernández-Rossier. Topological magnons in cri _3 monolayers: an itinerant fermion description. *arXiv preprint arXiv:2002.00077*, 2020.

[21] Inhee Lee, Franz G Utermohlen, Daniel Weber, Kyusung Hwang, Chi Zhang, Johan van Tol, Joshua E Goldberger, Nandini Trivedi, and P Chris Hammel. Fundamental spin interactions underlying the magnetic anisotropy in the kitaev ferromagnet cri 3. *Physical Review Letters*, 124(1):017201, 2020.

[22] Ryuichi Shindou, Ryo Matsumoto, Shuichi Murakami, and Jun-ichiro Ohe. Topological chiral magnonic edge mode in a magnonic crystal. *Physical Review B*, 87(17):174427, 2013.

[23] Ryuichi Shindou, Jun-ichiro Ohe, Ryo Matsumoto, Shuichi Murakami, and Eiji Saitoh. Chiral spin-wave edge modes in dipolar magnetic thin films. *Physical Review B*, 87(17):174402, 2013.

[24] M Zahid Hasan and Charles L Kane. Colloquium: topological insulators. *Reviews of modern physics*, 82(4):3045, 2010.

[25] Ryo Matsumoto, Ryuichi Shindou, and Shuichi Murakami. Thermal hall effect of magnons in magnets with dipolar interaction. *Physical Review B*, 89(5):054420, 2014.

[26] Benedetta Flebus, Ka Shen, Takashi Kikkawa, Ken-ichi Uchida, Zhiyong Qiu, Eiji Saitoh, Rembert A Duine, and Gerrit EW Bauer. Magnon-polaron transport in magnetic insulators. *Physical Review B*, 95(14):144420, 2017.

[27] Ch Kittel. Interaction of spin waves and ultrasonic waves in ferromagnetic crystals. *Physical Review*, 110(4):836, 1958.

[28] Michael P Marder. *Condensed matter physics*. John Wiley & Sons, 2010.

[29] Charles Kittel and Ching-yao Fong. *Quantum theory of solids*, volume 5. Wiley New York, 1963.

[30] Simon Streib, Nicolas Vidal-Silva, Ka Shen, and Gerrit EW Bauer. Magnon-phonon interactions in magnetic insulators. *Physical Review B*, 99(18):184442, 2019.